AIAA JOURNAL
Vol. 62, No. 7, July 2024

Evaluating an Additive Manufactured Acoustic Metamaterial Using the Advanced Noise Control Fan

Eoghan P. Ross*
The University of Dublin, Dublin D02 PN40, Ireland
Kelvin M. Figueroa-Ibrahim† and Scott C. Morris‡
University of Notre Dame, South Bend, Indiana 46556
Daniel L. Sutliff§
NASA Glenn Research Center, Cleveland, Ohio 44135
and
Gareth J. Bennett¶
The University of Dublin, Dublin D02 PN40, Ireland

https://doi.org/10.2514/1.J063384

This paper examines the performance of a 3D printed acoustic metamaterial as an acoustic treatment for aircraft engine nacelles in the Advanced Noise Control Fan. As the level of air travel continues to increase, so too does the demand for better noise-reduction technologies for aircraft. Engines are one of the two main sources of noise generated by aircraft, with fan noise, in particular, being of concern due to its broadband and tonal contributions. Small and lightweight methods of addressing both broadband and tonal noise are necessary due to the limitations presented by the current engine design. Presented in this paper is a novel acoustic metamaterial that has undergone design optimization for broadband noise reduction. The final design was produced using 3D printing and tested using the Advanced Noise Control Fan at the University of Notre Dame. It was found that the material is capable of reducing the first harmonic of the blade passing frequency by up to 18.5 dB, with an overall noise reduction of 3.7 dB.

Nomenclature

B	=	number of blades
c_0	=	speed of sound in air, ms^{-1}
H	=	Advanced Noise Control Fan centerbody height, m
H_{12}	=	transfer function
J_n	=	nth-order Bessel function
PWL	=	sound power level
p_t	=	total pressure, Pa
p_0	=	incident pressure, Pa
R	=	Advanced Noise Control Fan microphone radial distance, m
r	=	reflection coefficient
SPL	=	sound pressure level, dB
TL	=	transmission loss, dB
Z	=	normal surface impedance, $Pa \cdot s \cdot m^{-3}$
z	=	specific acoustic impedance, $Pa \cdot s \cdot m^{-1}$
α	=	absorption coefficient
θ	=	Advanced Noise Control Fan microphone polar angle
ν_0	=	kinematic viscosity of air, $m^2 \cdot s^{-1}$
τ	=	transmission coefficient
Φ	=	porosity
ϕ	=	Advanced Noise Control Fan microphone azimuthal angle
$\psi(\phi)$	=	Fok function
ω	=	angular frequency, $rad \cdot s^{-1}$

I. Introduction

As AIR travel continues to become more frequent, the demand on the industry to improve the efficiency of aircraft increases. While the aviation industry was greatly impacted by restrictions implemented during the pandemic, a report by Hasegawa [1] stated that annual numbers of air passengers would return to 88% of the 2019 levels by the end of 2022 and would exceed the 2019 levels by 2024 [2]. For those living in close proximity to airports and aviation centers, the return to normal air traffic levels and the anticipated increases will see a return to high levels of noise pollution. These levels of noise pollution have been seen to have a significant impact on the environment and populations in the surrounding areas. In recent years, aircraft noise has been the subject of a number of studies that have linked noise to numerous health problems, including cardiovascular diseases, non-Hodgkin lymphoma, and hypertension, as well as learning and developmental problems in young children [3–6]. Organizations such as the International Civil Aviation Organization (ICAO) and the Advisory Council for Aviation Research and Innovation in Europe (ACARE) have taken steps to address the problem of aircraft noise pollution [7]. The European Union introduced a number of regulations to reduce the impact of aviation on surrounding communities. Vision 2020, for example, required that by 2020 the perceived noise level from aircraft must be reduced by 50% compared to standard levels in 2000. Flightpath 2050 continues on from Vision 2020 and seeks to reduce the perceived noise emissions from aircraft by 65% compared to 2000 standard levels by 2050 [8].

Approaches to reducing aircraft noise are typically split into two categories: airframe [9–11] and engine noise reduction. The introduction of the turbofan engine and its associated bypass resulted in a significant reduction in aeroengine noise when compared to the jet engine predecessors [12–14]. However, with the introduction of the turbofan engine came a new source. While the overall engine noise output, especially from the jet, was significantly reduced, fan noise was introduced, which contains high levels of both broadband and

Presented as Paper 2023-3827 at the AIAA Aviation Forum 2023, San Diego, CA, June 12–16, 2023; received 14 July 2023; revision received 21 February 2024; accepted for publication 24 February 2024; published online Open Access 26 April 2024.

*Graduate Student, Department of Mechanical, Manufacturing and Biomedical Engineering, Trinity College Dublin. Member AIAA.

†Graduate Student, Department of Aerospace and Mechanical Engineering.

‡Professor, Department of Aerospace and Mechanical Engineering. Senior Member AIAA.

§Aerospace Engineer, Acoustics Branch, MS 54-3, 21000 Brookpark Road. Associate Fellow AIAA.

¶Associate Professor, Department of Mechanical, Manufacturing and Biomedical Engineering, Trinity College Dublin; gareth.bennett@tcd.ie. Senior Member AIAA (Corresponding Author).

tonal noise. With the continuing development of ultra-high-bypass (UHBP) ratio engines, motivated by fuel efficiency and emissions reduction, these fan noise components are moving to increasingly low frequencies [15]. In addition, in principle, an UHBP ratio fan will result in an increased nacelle diameter and a heavier engine. This consequence can impact liners in two ways: 1) the liner depth may need to be reduced to prevent the larger-diameter nacelle from rubbing the ground; 2) the length of the nacelle, and thus the liner, may need to be reduced in length in order to reduce weight. Both cases require that smaller, more lightweight, and correspondingly more efficient noise-absorbing technologies be developed.

The current industry standard for nacelle liners is generally a perforated panel over honeycomb liner in either single or double degree-of-freedom configuration (SDOF/DDOF). The design is lightweight and strong due to the structural strength of the honeycomb core. Each duct within the honeycomb design acts as a quarter-wavelength resonator, a Helmholtz resonator, or a combination of both. These duct resonators are efficient at absorbing sound, but in a relatively narrow frequency band, which is a function of either the duct's length or volume [16]. The DDOF liner adds a second duct depth to the liner in order to add a second characteristic absorption peak to broaden the liner's overall absorption response. To achieve low-frequency attenuation, the depth of the liner must be increased. However, as the depth of the liner is increased the frequency response of the liner narrows, and typically the absorption coefficient decreases. Combined with the growing constraints on the size of the liners, an alternative approach to engine liner development must be explored, which can lower and broaden the frequency response as well as increase the absorption response.

Acoustic metamaterials (AMMs) hold significant promise for the next generation of engine nacelle liners. Artificially designed and engineered, AMMs typically exhibit effective properties different from those expected from their physical properties. A variety of different approaches are used when designing AMMs, including space coiling, lattice structures such as Kelvin cells, decorated membranes [17–19], acoustic plates [20], and hybrid technologies [21]. These different approaches each have a focus that allows a specific property to be obtained by manipulating the effective properties of the material. Many of these approaches have been investigated in the case of normal incidence, in which the incident acoustic wave is normal to the active surface of the metamaterial [22–26]. However, for use as a nacelle liner, the performance of the material in grazing incidence is of greater interest as the liner must not interfere with the airflow through the engine. Depending on the publisher, some types of AMM could also be described as advanced multi-degree-of-freedom (AMDOF) liners, which is the case with the technology discussed in this paper. The application of AMDOF liners and similar technologies in grazing incidence has been investigated by NASA Langley using the Grazing Flow Impedance Tube, as well as in a number of other laboratories, including LAUM in Le Mans, KTH, DLR, and JAXA [27–31]. In addition, advanced inlet MDOF liners with "mesh-cap" septa fabricated from PEEK have been evaluated in nacelles and in full flight tests [32–35]. However, to the author's best knowledge, results from testing *3D printed* advanced MDOF technologies in an engine nacelle have yet to be published.

The current study reports the design and manufacture (3D printing) of an AMM/AMDOF absorber that was optimized for normal impedance and produced very successful results. The technology was subsequently evaluated as an inlet liner in the Advanced Noise Control Fan (ANCF). The ANCF [36] is well known to aeroacoustics researchers, having been involved in many research campaigns while located at NASA Glenn. It now resides at the University of Notre Dame and continues to be used as a research and development tool. The AMDOF absorber was optimized for normal acoustic incidence and not grazing acoustic incidence with flow. However, it was observed that high-amplitude acoustic output from the ANCF rig coincided, in the frequency range, with the high attenuation range of the absorber. As the ANCF rig runs at both relatively low Mach numbers and with relatively low output sound levels, it was considered reasonable to expect the AMDOF absorber to perform similarly in both rigs. At least, it was worth evaluating with a view to further developing the design in future research if the results were positive. The AMDOF absorber was 3D printed into 237 blocks of 50 mm depth (2 inches) and inserted into the inlet casing of the ANCF to form an inlet sound-absorbing liner targeting noise below 4 kHz.

II. Experimental Setup

The experimental approach consisted of three experiment types on two different experimental rigs. The first rig is an impedance tube at Trinity College Dublin that can be used to evaluate normal acoustic incidence properties as well as transmission loss under grazing acoustic incidence without flow. The second test campaign took place using the ANCF rig at the University of Notre Dame to assess the capacity of the AMDOF absorber to perform as an aeroengine acoustic liner. The AMM design is considered to have a low technology readiness level (TRL) as the 3D printed parts are made of plastic, suiting the cold-flow operation of the ANCF. The primary objective was to evaluate the design, which, if successful, could lead to further research into more suitable materials for aeroengines.

A. Grazing Incidence Impedance Tube in Trinity College Dublin

The Grazing Incidence Impedance Tube (GIIT) at Trinity College Dublin is a multipurpose rig that can be used for grazing acoustic impedance eduction, transmission loss testing in accordance with ASTM E2611-09 [37], and normal acoustic impedance measurements in accordance with ISO 15034-2:2001 Standard [38]. The rig does not facilitate mean flow, and thus when the test sample is located on a lateral duct wall, it only examines grazing *acoustic* incidence (Fig. 1).

The GIIT is designed for SPL testing of up to 130 dB. The walls of the tube are aluminum, measuring 0.015 m in thickness. The tube has an internal rectangular cross section of 0.05 m in the spanwise dimension and 0.08 m in height. A 0.45 m × 0.05 m cutout is centered in the lower panel of the tube to facilitate grazing acoustic incidence testing. Sample depths of up to 50 mm are typically tested. The tube measures 1.75 m in length from the acoustic source to the termination. The acoustic source is two BMS 4591 compression drivers mounted opposite each other in the top and bottom walls of the tube. The frequency range of the drivers is between 200 Hz and 9 kHz, and thus the lower limit of the rig is 200 Hz. There are 22 microphone mounts in the upper wall of the tube; 20 microphone mounts are for grazing incidence tests, and the final two are located near the termination, N_1 and N_2, located 0.23 and 0.16 m from the termination,

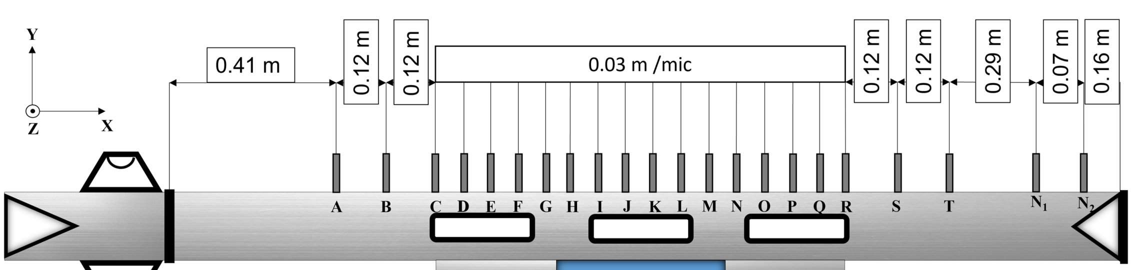

Fig. 1 Design of the GIIT in grazing acoustic incidence configuration.

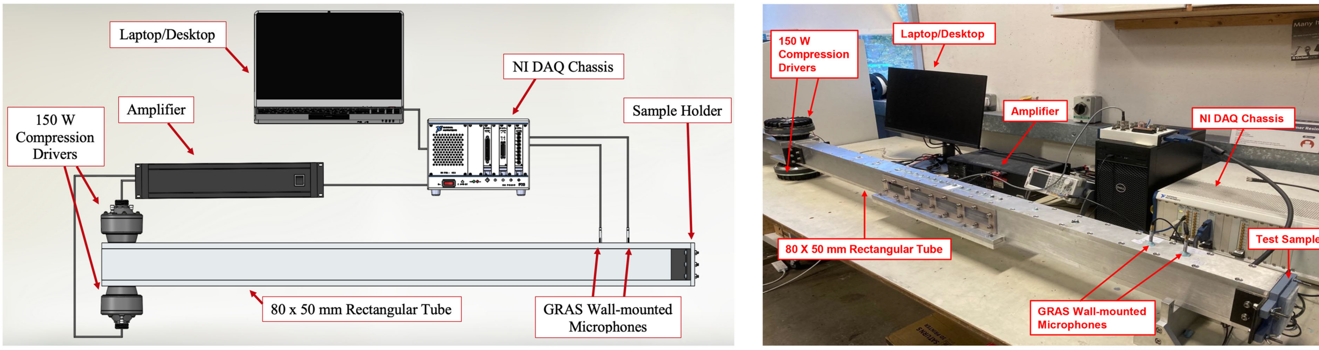

a) Schematic of the GIIT **b) Photo of GIIT and Data acquisition system**

Fig. 2 GIIT setup for normal incidence testing.

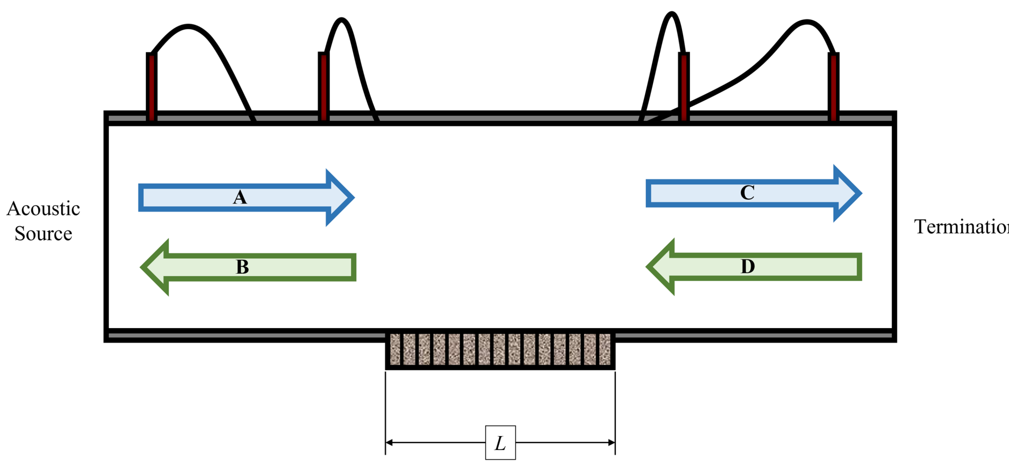

Fig. 3 The transmission coefficient is determined using the four waves superimposed upstream and downstream of the acoustic sample as shown.

respectively, are used for the normal incidence tests (Fig. 2). The microphones used in the measurements were G.R.A.S. 40PH microphones. The 40PH has a flat frequency response from 20 Hz to 20 kHz. Further details on the rig can be found in Ref. [39].

Figure 3 shows the simplified schematic to illustrate how the grazing transmission loss was calculated. The transmission coefficient τ of a material is the ratio of the transmitted sound pressure at the opposite end of the acoustic sample to the incident sound pressure. This requires four measurement points to be used: two upstream of the sample and two downstream. Microphones A, B, S, and T in Fig. 1 were used for this purpose. Additionally, the measurement as outlined in ASTM E2611-09 [37] requires the wave to be measured with two termination conditions: anechoic and hardwall.

Four acoustic waves were therefore recorded to determine the transmission coefficient: A) the incident wave, B) the reflected wave, C) the transmitted wave, and D) the reflected transmitted wave. These four waves can be seen in Fig. 3. As the measurement is performed twice, there are two sets of each of these four waves. The waves measured in the anechoic configuration are denoted with the subscript o, and the waves in the hardwall configuration are denoted with the subscript h. The transmission coefficient is given by

$$\tau = \frac{A_o D_h - A_h D_o}{C_o D_h - C_h D_o} \tag{1}$$

where each of A, C, and D refers to the transfer function for each wave of the same label. Using the transmission coefficient, it is possible to determine the transmission loss

$$TL = -20\log_{10}\left(\frac{1}{\tau}\right) \tag{2}$$

in which TL is the transmission loss, given in decibels.

B. Advanced Noise Control Fan

The ANCF was designed in the early 1990s and envisaged as a testbed for fan noise reduction technologies. It was designed to be a low-cost, low-technology readiness-level (TRL) experimental rig. In addition to its role in aiding the development of fan noise reduction technologies, it has also served to further the understanding of aeroacoustic physics and code validation. In the over 20 years of its lifetime, the ANCF has been upgraded a number of times and most recently relocated from the NASA Glenn Research Center to the Turbomachinery Laboratory at the University of Notre Dame [36].

The ANCF is a duct fan that has a 1.22 m (4 ft) internal diameter. The duct is highly configurable with ring sections that are capable of being moved to obtain the desired duct geometry or having hardwall sections replaced with liner sections for testing. These sections can be seen in Fig. 4. The nominal operational speed of the ANCF is 1800 revolutions per minute (RPM), with a range of 100–2400 RPM. At the nominal operating speed, the fan tip speed is approximately 115 ms^{-1}, the inlet Mach number is approximately 0.15, and the fundamental blade passing frequency (BPF) is approximately 500 Hz. The ANCF rotor has 16 blades with a nominal pitch angle of 28°, though it can additionally be set to 18° or 38°. It is possible to run the ANCF in a rotor-only configuration, or with a stator stage attached downstream of the rotor. The stator count is variable, and it is capable of being set to any angle. An inlet control device (ICD) is installed at the front of the ANCF, which is used during static ground tests in order to condition the airflow into the duct. The ICD conditions the airflow by breaking up large vortices and reducing the size of the structures in the flow, which would otherwise become an additional noise source in the duct. The ICD is a layer of honeycomb sandwiched between two layers of fine mesh, installed in 22 longitudinal sections [36].

The performance of the ANCF in these tests is considered to be within the linear range, as confirmed by previous tests. The ANCF

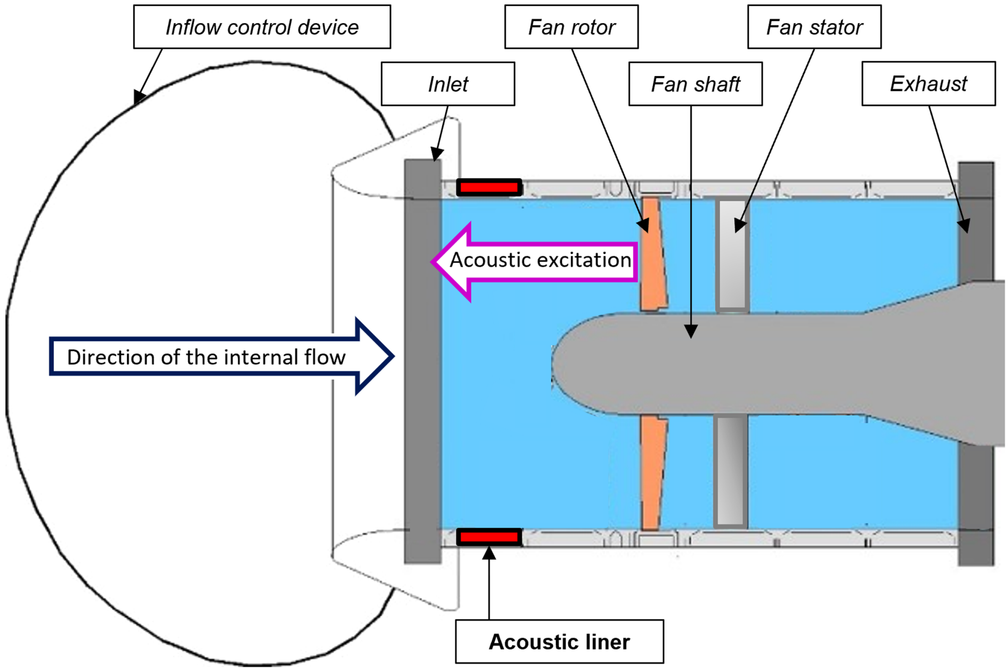

Fig. 4 Schematic of the ANCF. Adapted from Sutliff [36].

has a low maximum Mach number of 0.3. Previous testing that has been performed during its time in the Aero-Acoustic Propulsion Laboratory at NASA Glenn using the in-duct rotating rake has indicated levels of up to 120 dB mode PWL. As the Mach number in the current tests was 0.15, it is expected that the in-duct SPL would be lower still, certainly within the linear range. As a consequence, it is considered that nonlinearity effects should not be significant when comparing the impedance tube results to the current ANCF tests. These values are significantly below the 150–160 dB mode PWL that would be seen in-duct in a full-scale engine. However, the assessment of the liner in such conditions is beyond the scope of the current research.

1. Far-Field Acoustic Measurements

Since the transfer to the University of Notre Dame, ANCF testing has been conducted outdoors at the White Field Facility [40]. The data acquisition is performed by an array of ground-based microphones. This array typically consists of 30 microphones, split into a fore array and an aft array, each containing 15 microphones. However, the primary focus of this study was on the capacity of the inlet liner to reduce the upstream propagating fan noise, and so a single fore array of all 30 microphones was used. The microphones were set up at a radius of 6.1 m (20 feet) from the ANCF. The microphones had a 3.2° spacing, spanning from the center line of the ANCF at 0° to just past the inlet plane at 93.2°. The setup can be observed in Fig. 5.

The 3.2° angle of separation between the microphones is the polar angle. As the outdoor test setup uses ground microphones for data acquisition, the microphones were not in the same plane as the ANCF shaft. To address this, the azimuthal angle is used for any calculations relating to the directivity of the noise and the power level calculations [40]. The azimuthal angle can be found using

$$\phi = \cos^{-1}\left(\frac{R * \cos(\theta)}{\sqrt{R^2 + H^2}}\right) \tag{3}$$

Fig. 5 ANCF setup at the White Field facility in the University of Notre Dame.

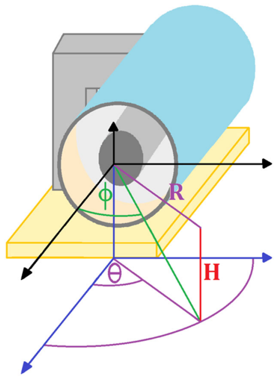

Fig. 6 Diagram of the relationship between the microphone polar angle θ and the azimuthal angle ϕ.

where ϕ is the azimuthal angle, θ is the polar angle, R is the radial distance from the inlet of the ANCF to the microphone, and H is the height of the ANCF center line from the ground. The angles θ and ϕ can be seen in Fig. 6.

Data acquisition was performed using an HMB GEN2i Data Recorder, which recorded the time series data from the 30-microphone array and the shaft rotation of the ANCF. The time histories were processed using ensemble averaging. An example of the resulting energy spectrum can be seen in Fig. 7a, where the y axis is plotted as a function of shaft order. As the ANCF test configuration used in this campaign had 16 blades, we see the BPF peak occurring at 16 shaft orders. Shaft revolution-triggered ensemble averaging allowed the total fan noise to be decomposed into tonal and broadband components. As an alternative to octave band analysis, for example, the data was further analyzed in terms of energy bands centered on the BPF or on its harmonics, viz., fan tones. These fan-tone-centered frequency bands are termed "harmonic bands." The first harmonic band is centered about the first fan tone (BPF). This occurs between $0.5B$ and $1.5B$, where B is the number of blades if considering the shaft order (see Fig. 7a). As can also be seen in Fig. 7b, the 1st harmonic band is centered on the 16th shaft order, spanning from the 8th to the 24th shaft order. Similarly, the remaining harmonic bands are centered around the remaining fan tone harmonics and are defined to be in the range $B(N \pm 0.5)$, where N is the harmonic band number in question. By integrating the harmonic bands, this approach can be used to independently analyze the three data sets, i.e., the overall (original) data, as well as the decomposed broadband and tonal data components as a function of the harmonic band (see Fig. 7c).

The data can be converted into the acoustic power level (PWL) by squaring the pressure and multiplying by the appropriate area, and then normalizing by the specific acoustic impedance. This is given by

$$\mathrm{PWL} = \frac{p^2 * A}{z} \tag{4}$$

where p is the acoustic pressure, A is the circular sector area between the microphones, and z is the specific acoustic impedance of air. The area is determined using the corrected azimuthal angle given in Eq. (3). This can be used to obtain the far-field acoustic data in terms of the overall, broadband, and tonal power components [41].

III. Design and Numerical Simulation

A. Concept

As discussed, the material being investigated is called, depending on the research community in question, an advanced MDOF absorber (aeronautics) or an AMM (applied physics). We will refer to it as the former, i.e., an AMDOF absorber, which is manufactured using additive manufacturing. This particular design builds on many concepts to be found in the literature, in particular the "hybrid acoustic metamaterial" of Tang et al. [42]. In their initial paper, the concept of a "honeycomb core" structure with two principle perforated layers was introduced, with the first perforated layer being a faceplate and the second being a perforated septum, which divides the core structure diagonally at various heights. The honeycomb core has a square cross section and will be referred to as simply the "core" structure in this study. It should be noted that the concept of a diagonal septum was also previously investigated by Parrott and Jones [43], where the septum was a wire mesh and not a perforated plate. In the work of Tang et al. [42], the concept was designed with the intention of metal fabrication: folded metal corrugations, etc. In our work, we advance the concept of additive manufacturing to control precisely important geometric parameters, which have been optimized, and to allow the absorber to be made as one single part.

Two methods of incorporating the septum were investigated in this study initially. Both approaches have a periodic design that repeats every six cells in the streamwise direction. The first is a diagonal septum, as seen in Fig. 8a. The second method has a horizontal septum, as seen in Fig. 8b. In both models, the general structure is the same. The first cell has a perforated septum at the top of the cell, and the fourth cell has a nonperforated septum at the bottom of the cell (a blind hole in the figure), which represents a solid metal partition in the original Tang design. While the diagonal and horizontal septa divide the remaining cells differently, the average height of the perforation in the septum is the same. In the second and sixth cells, the perforation is at 3/4 the height of the cell; in the third and fifth cells, the perforation is at 1/4 the height of the cell. Figure 8 also shows a basic single hole per duct faceplate for illustration purposes only. The design of the faceplate, as well as the core, is subject to an optimization process with the objective of maximizing acoustic absorption.

As the material being investigated in this work is produced using additive manufacturing, a number of design and manufacturing limitations introduced by traditional manufacturing methods do not apply. The use of the single corrugated layer in the Tang design to divide the honeycomb core, for example, is not necessary as the additive manufacturing process allows horizontal septa to be used instead. However, 3D printing a horizontal septum is not straightforward, as the correct printing settings need to be determined and calibrated, and an appropriate angle for the part needs to be chosen to overcome difficulties in printing a surface that will have no support scaffolding. Scaffolding could not be accommodated, as there would be no way to remove it. The flat surface of our septum has the advantage of a more uniform and well-defined perforation compared to drilling at an angle through a diagonal sheet of metal. In this work,

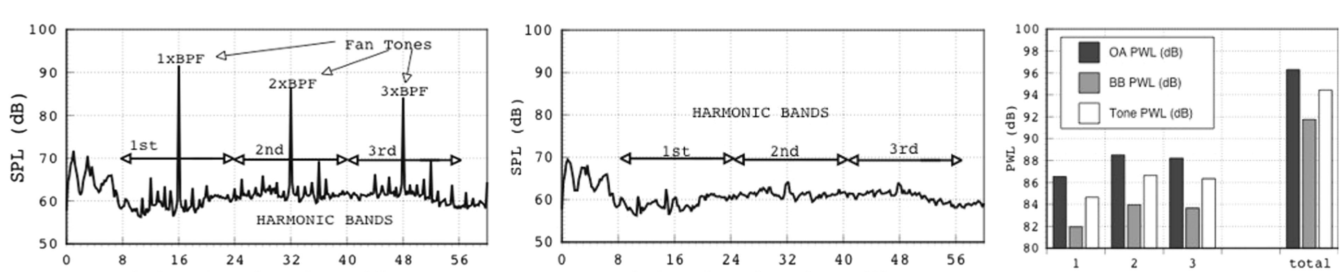

a) Original spectral sample **b) Broadband spectral sample** **c) Harmonic bands PWL**

Fig. 7 Example of the far-field data reduction into broadband and harmonic bands. Reprinted in part from [41].

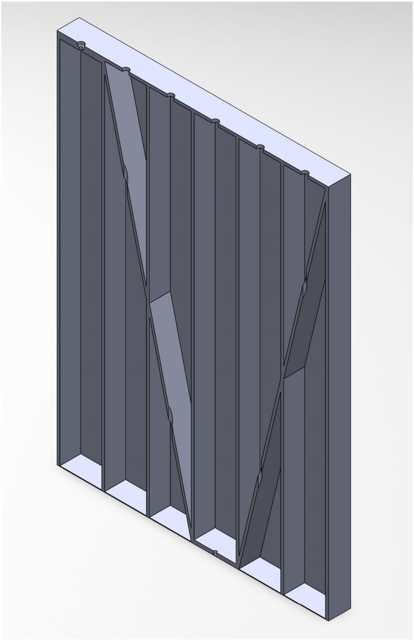

a) Design featuring a diagonal septum

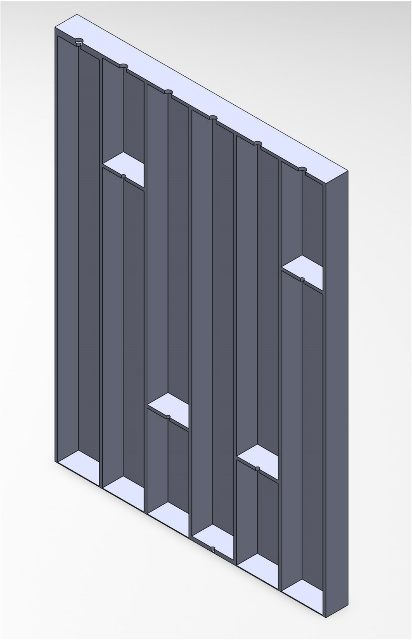

b) Design featuring a horizontal septum

Fig. 8 Cross section of the design concept for the liner core configurations investigated. Basic single-hole faceplate shown.

to differentiate it from other samples we test, we refer to this single-piece, optimized, 3D printed AMDOF absorber that we have developed and evaluated as the “T-Liner” (“T” for Trinity).

B. Finite Element Model

A full 3D FEM numerical analysis of the normal impedance experimental work conducted using the GIIT was implemented in the frequency domain. The simulations were performed using COMSOL Multiphysics® version 6.0 with the Acoustics module. Preliminary work and investigations in normal incidence were conducted using a single unit cell. The single-unit cell is a one-by-six array of ducts, as seen in Fig. 9, which is similar to Fig. 8 but without the basic faceplate.

1. Meshing

The meshing was performed with a user-controlled mesh. For acoustic meshing within COMSOL, it is recommended to have at least 6–8 mesh elements per wavelength, so the maximum element size was set at 1/8th of the smallest acoustic wavelength of interest, λ_0. The minimum element size was set at 1/3rd of the viscous boundary-layer thickness, $d_{\text{visc}} = 220\ \mu\text{m} * \sqrt{(100\ \text{Hz}/f_0)}$.

The model was meshed with a combination of swept mesh elements in duct sections, boundary-layer meshing in the microperforated holes, and free tetrahedral mesh elements in the duct region directly above the sample. The swept mesh extrudes the surface mesh of a boundary through the domain. If a domain has different, complex geometries at either end of the domain or a nonplanar boundary, a swept mesh cannot be used. When a swept mesh is required for a domain with incompatible end boundaries, a domain partition is used to create a transition zone. An example of this can be seen in Fig. 10a. By partitioning the domain, the larger section can be meshed using a swept mesh first. A free tetrahedral mesh can then be used in the smaller domain, which has two different end boundaries. The boundary-layer meshing used in the perforations can be seen in Fig. 10b.

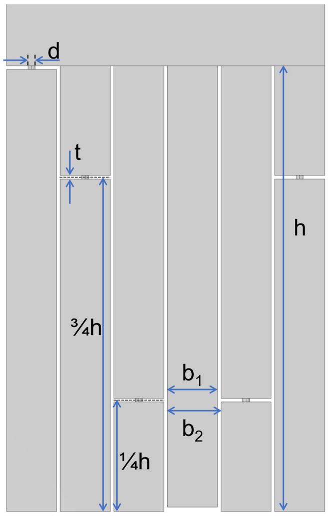

Fig. 9 Midplane section view of the unit cell of the liner core. Shown are the geometry and parameters of the initial design used in the parametric study; *d* and *t* are the variables to optimize.

2. Estimation of the Absorption Coefficient

To calculate the reflection and absorption coefficients in COMSOL, a frequency domain study with a 5 Hz step size was applied to the model. The frequency range used in the study was between 200 Hz and 2 kHz to match the plane-wave frequency range of the GIIT. Further details on the method can be found in Ref. [39].

IV. The 3D Printed “T-Liner” Design Optimization and Manufacture

The objective of the study was to design a novel AMDOF absorber optimized for noise attenuation over a wide frequency range. In order to quantify its performance, it was compared to a standard 50 mm (2″) single-degree-of-freedom honeycomb liner that was considered the benchmark. In order to have a fair comparison, the benchmark was also optimized for maximum performance. As the performance of the honeycomb backing, or “core,” is only a function of its depth, only its faceplate has the capacity for optimization. The procedure for the optimization is detailed below and requires a measure of the impedance of the core, which can be measured experimentally in the impedance tube or else, for this simple honeycomb case, can be provided analytically with the usual cotan function expression.

Similarly, the optimization of the T-Liner was broken into two stages. The first was the optimization of its core, which we call

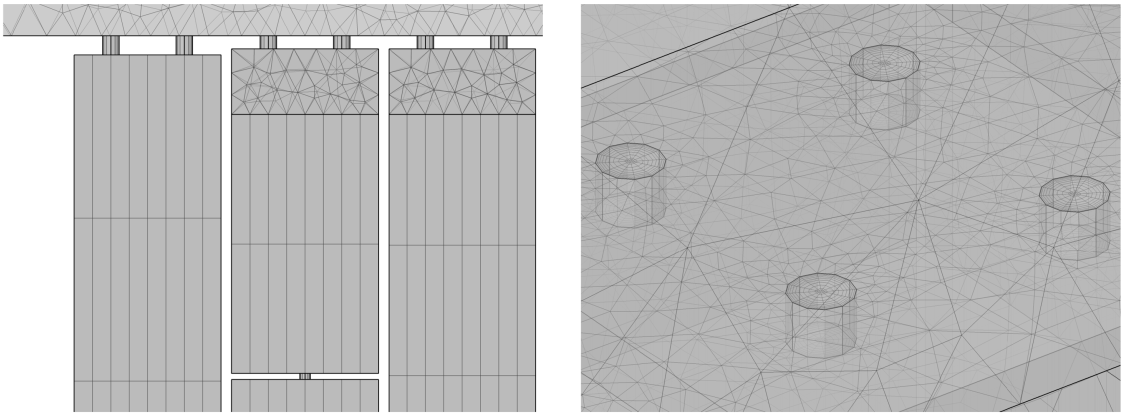

a) Side-view of liner with different mesh elements used

b) Isometric-view of mesh with boundary layer meshing in the perforations

Fig. 10 Different mesh element types are used to mesh different domains in the acoustic sample.

"parameterization." Once the parametric study of the core was complete, due to its complexity, its impedance was measured experimentally in the impedance tube, and this value was used as an input in order to optimize its matching faceplate. As we use an experimentally determined value of impedance, this is a semi-empirical method.

Figure 11 shows a schematic of the multistage optimization process used to optimize the liner geometries.

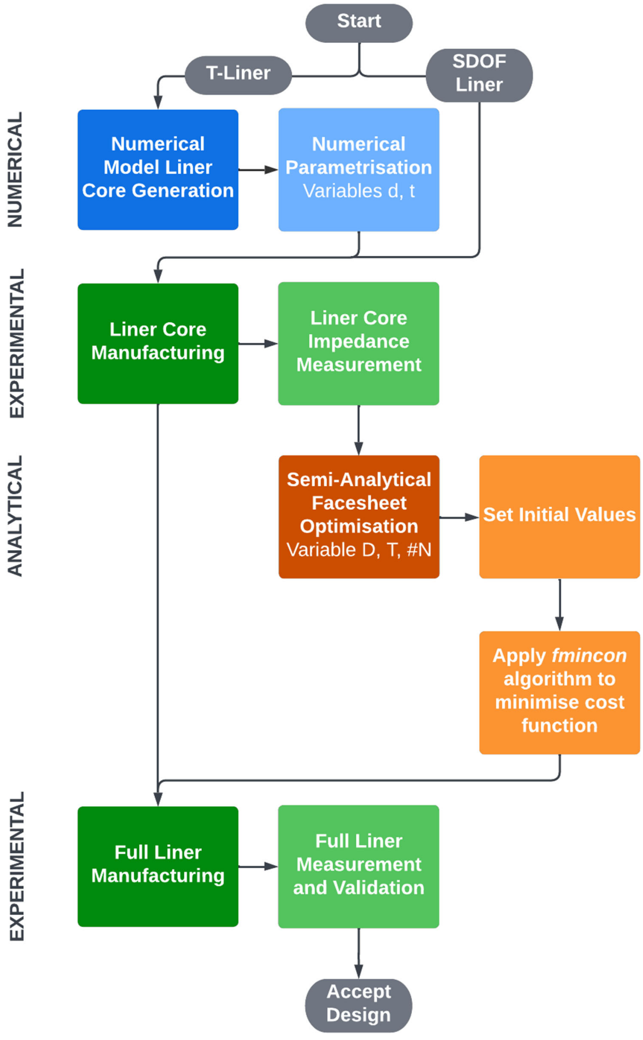

Fig. 11 Multistage optimization process used to optimize the liner geometry.

A. T-Liner Core Parametric Study

The objective of the parametric study was to determine the value of the thickness of the septa in the ducts, t, and the diameter of the perforations in the septa, d, which would provide the highest average value of absorption over a frequency range. The parametric study fixed the width of the honeycomb walls, the width of the honeycomb ducts, and the height of the core. These values can be found in Table 1, and the geometry can be seen in Fig. 9. In the parametric study, only the liner core is being parameterized without the faceplate, which means that five of the six ducts seen in Fig. 9 are fully open at the top. Only the first duct has a faceplate with a perforation of diameter d.

The parametric study was conducted using both COMSOL and MATLAB. A model similar to that in Fig. 9 was created in COMSOL, and the absorption coefficient with a septum thickness and perforation diameter of 0.2 mm was calculated at 200 Hz and saved to MATLAB. The septum thickness was incremented by the step size found in Table 2, and the absorption coefficient using COMSOL was found again. The process was repeated iteratively for all values of septum thickness and perforation diameter for the full frequency range in steps of 5 Hz. The full set of results was processed in MATLAB, and the optimal parameters for the maximum absorption coefficient were determined. The frequency sweep across this range of values took 10 days for each core configuration studied. The liner core configuration with the highest mean absorption was the horizontal septum configuration, with a septum thickness of $t = 0.2$ mm and a perforation diameter of $d = 0.4$ mm. The mean absorption of this liner core was calculated to be $\bar{\alpha} = 0.53$ in the 200 Hz–2 kHz frequency range. The experimentally measured impedance and absorption of the optimized liner core structure can be seen in Fig. 12.

Table 1 Fixed parameters of the liner core geometry

Parameter	Value
Cell width (b_1), mm	5.6
Wall thickness ($b_2 - b_1$), mm	0.4
Total height of core (h), mm	50

Table 2 Ranges for the parametric study

Parameter	Septum thickness (t), mm	Perforation diameter (d), mm
Minimum	0.2	0.2
Maximum	0.4	0.8
Step size	0.025	0.02

B. Faceplate Optimization

A 3D printed prototype of the liner core was produced using the design parameters identified in the parametric study. The normal impedance of this liner core was experimentally measured using the GIIT, shown in Fig. 12a, and used in the semi-analytical optimization routine in order to determine the optimized faceplate parameters. The routine is based on the analytical solution of a microperforated panel (MPP), as described by Maa [44]. In their paper, Maa [44] describes how the depth of a basic cavity is used as the reactive component of the impedance, and the resistance is determined from the geometry of the faceplate. The basic cavity reactance is defined by its depth using the cotangent function [44]. As the T-Liner core structure is more complex than a basic cavity, its experimentally measured impedance is used as an input, which replaces the analytical solution for the backing impedance. The experimentally measured impedance contains both a resistive and a reactive component. The total acoustic impedance of the T-Liner is therefore given by

$$Z = Z_{\mathrm{MPP}} + Z_C \tag{5}$$

in which Z_{MPP} is the acoustic impedance of the microperforated plate and Z_C is the acoustic impedance of the liner core. The acoustic impedance of a microperforated plate is given by

$$Z_{\mathrm{MPP}} = -Z_0\left(\frac{i\omega_0}{c_0\Phi}\frac{J_0\left(\frac{D}{2}\sqrt{\frac{-i\omega_0}{\nu_0}}\right)}{J_2\left(\frac{D}{2}\sqrt{\frac{-i\omega_0}{\nu_0}}\right)}[T + 0.85D\cdot\Psi(\phi)]\right) \tag{6}$$

where Φ is the porosity of the microperforated plate, J_0 and J_1 are the zeroth- and first-order Bessel functions, and ν_0 is the kinematic viscosity of air. The values T and D are the plate thickness and perforation diameter, respectively [17]. Finally, $\Psi(\phi)$ is the Fok function, which is used to determine the hole-to-hole interactions [45] and is given by

$$\Psi(\phi) = \sum_{n=0}^{a} a_n\left(\sqrt{\phi}\right)^n \tag{7}$$

where the first nine coefficients a_n that are used in this study are given by McKay et al. [17].

The optimization routine was used to determine the faceplate geometry, i.e., hole diameter, plate thickness, and porosity, to maximize the total absorption of the device for the given core impedance. This allowed an optimized faceplate to be generated for each core used in the study.

The specific acoustic impedance of the core and faceplate can be represented by

$$z = A\left(Z_{\mathrm{MPP}} + Z_{\mathrm{exp}}\right) \tag{8}$$

where A is the surface area of the device and Z_{exp} is the experimentally measured acoustic impedance. Using the specific acoustic impedance of the device, the absorption coefficient is

$$\alpha = 1 - |r|^2 = 1 - \left|\frac{z - z_0}{z + z_0}\right|^2 \tag{9}$$

where r is the reflection coefficient and z_0 is the characteristic specific acoustic impedance of air.

To maximize the absorption coefficient of the device, a cost function is defined to find the average absorption in the frequency range of interest:

$$-\bar{\alpha} = -\frac{1}{f_2 - f_1}\int_{f_1}^{f_2} \alpha\,\mathrm{d}f \tag{10}$$

The optimization is performed in MATLAB using the *fmincon* algorithm that is used. The negative value of the mean absorption is used in the cost function as the algorithm aims to minimize the cost function, but the aim of the optimization is to maximize the absorption coefficient. It is possible to apply a frequency weighting in the cost function if there is a particular frequency or frequency range that is to be targeted [18,19,46,47]. In this study, frequency weighting was not used as the device was being optimized for general use in the sub-2-kHz range. The limits of f_1 and f_2 were set to 200 Hz and 2 kHz, the operational range of the GIIT in TCD.

Related to the porosity, the optimization routine was also used to determine the number of perforations, *#N*, in the faceplate. As the part was 3D printed, precise control over the location of the perforations was possible. Quite often in liner design, the location of the perforations relative to the honeycomb ducts can be arbitrary, with holes often aligning with the duct wall, rendering it ineffective. In this study, a fixed number of holes located over each duct was used as opposed to having the total number of holes be unconstrained. Three values for the number of perforations were used: 104 (1 hole per cell), 416 (4 holes per cell), and 936 (9 holes per cell). The remaining options used in the optimization are given in Table 3.

The final design for the faceplate provided by the multistage optimization process had a thickness $T_2 = 0.5$ mm, a perforation diameter $D = 0.63$ mm, and 416 perforations, 4 holes per cell, in the faceplate. This configuration for the optimized faceplate and liner core had a theoretical mean absorption of $\bar{\alpha} = 0.72$, highlighting

Table 3 Ranges for the analytical optimization

Parameter	Faceplate thickness (T_2), mm	Perforation diameter (D), mm
Minimum	0.2	0.3
Maximum	0.9	1.0

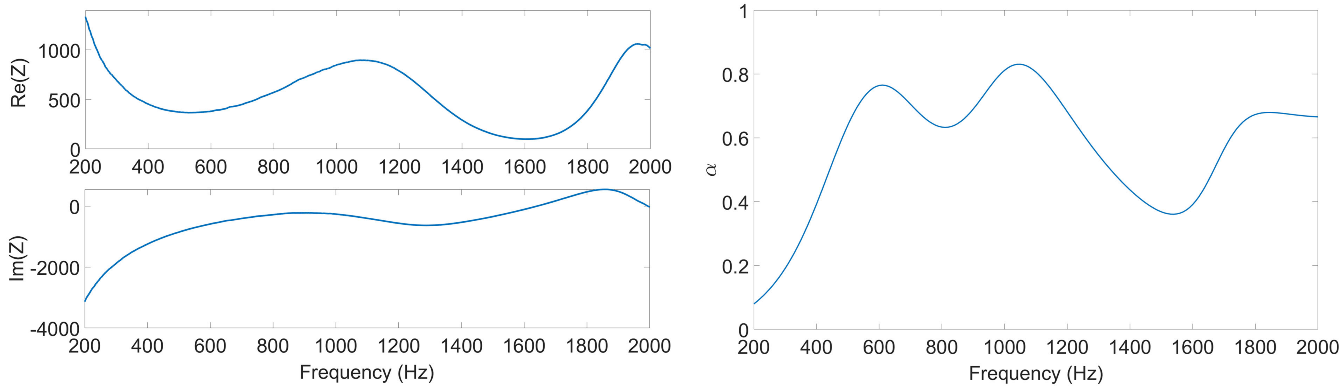

a) Impedance of the liner core **b) Absorption of the liner core**

Fig. 12 Experimentally measured impedance and absorption of the T-Liner core structure.

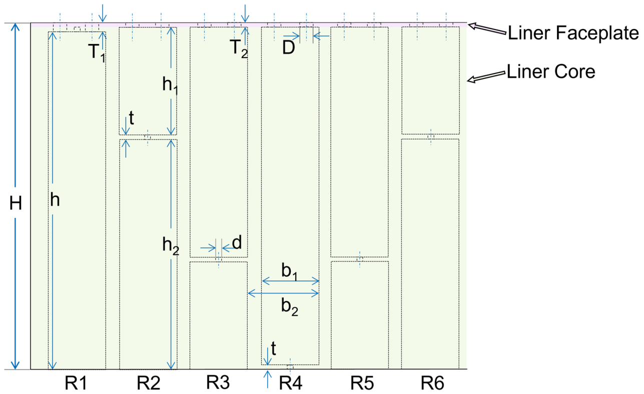

Fig. 13 Geometry of the final T-Liner design with a horizontal septum.

Table 4 Final parameters

Parameter	Value, mm
Total core height, h	50
Upper duct height, $h_{1,R2}$	12.35
Lower duct height, $h_{2,R2}$	37.25
Duct internal width, b_1	5.6
Duct total width, b_2	6
Faceplate thickness, T_2	0.5
Septum thickness, t	0.2
Faceplate perforation diameter, D	0.63
Faceplate perforation count, N	416
Septum perforation diameter, d	0.4

the benefit of adding a faceplate to the core structure. The final design configuration can be seen in Fig. 13, and the parameters are summarized in Table 4. The experimentally measured impedance and absorption of the optimized T-Liner can be seen in Fig. 14.

C. Manufacturing

All printers used in this work were masked stereolithography (MSLA) printers. Stereolithography is a form of additive manufacturing often used for fast prototyping, particularly when the prototype involves small features. It uses a liquid resin photopolymer that can be cured when exposed to UV light. The cured resin forms very thin, solid layers that stack to form the object. Masked stereolithography uses an LED and LCD photomask to produce the pattern for each layer. The LED array is located below the LCD photomask display. The entire LED array illuminates for every layer, but the LCD photomask deactivates individual pixels to produce the pattern for each layer, which allows the LED light to pass through [48]. As the MSLA light source is an array, the power passed through each pixel of the LCD photomask is the same, resulting in a more uniform build quality. An example of the generated print file for the T-liner can be seen in Fig. 15. Also seen, in gray, is the support tree, which is support scaffolding used during additive manufacturing to print over an area of "free space," meaning that there is no material in that area on the previous layer. Support structures are designed to be easily removed, and any traces that remain can be removed by lightly sanding the surface. In order to mitigate any impact on the performance of the liner, the supports are only attached to the sides of the liner that are not acoustically active. For the final testing, additional spacing was allowed so that samples could be sanded down to the required size to install in the ANCF.

An image of the MSLA 3D printed final design of our original 3D printed "T-Liner" can be seen in Fig. 16 from two perspectives.

D. ANCF Adaptation

The T-Liner was installed in the inlet liner casing of the ANCF for testing, as seen in Fig. 17. The casing has a rectangular cross section in the circumferential direction with a streamwise length of 228.6 mm and a radial depth of 57 mm. The depth of the T-Liner acoustic absorber was kept at 50.5 mm to keep the expected frequency response consistent with the testing conducted using the GIIT. The remaining depth in the casing was filled using the standard carpet padding between the casing wall and the base of the material. The final liner design consisted of six full unit cells and one repetition of the R1 cell in the streamwise direction and eight cells in the circumferential direction, as can be seen in Fig. 18. The additional R1 cell was included to make the design symmetrical in the streamwise direction. The blocks were 3D printed in three parts due to limitations in the size of the printer's print bed. The different colors of the blocks simply correspond to the color of the resin available and have no further significance beyond that. Further details can be found in the thesis of Ross [49].

To account for the curvature of the casing, the geometry of the blocks tested in the GIIT needed to be slightly adjusted so that the curvature of the faceplate would match that of the ANCF inner wall, which has a diameter of 1.22 m (4 ft). This can be seen in Fig. 18. It is assumed that the slight curvature will not have a significant impact on the impedance of the liner. The width at the top of the cell was kept constant, and the width at the base was increased. Each part, eight cells wide, spans 4.6°. This is approximately 50 mm measured at the top of the part and takes into account the approximate expansion of the printed parts. Seventy-nine parts were therefore required in the circumferential direction to fill the casing, and as 3 were needed in the streamwise direction, this meant that 237 were needed in total. Adjoining block walls were printed with a thickness such that splices were approximately equal to the distance between perforations and so

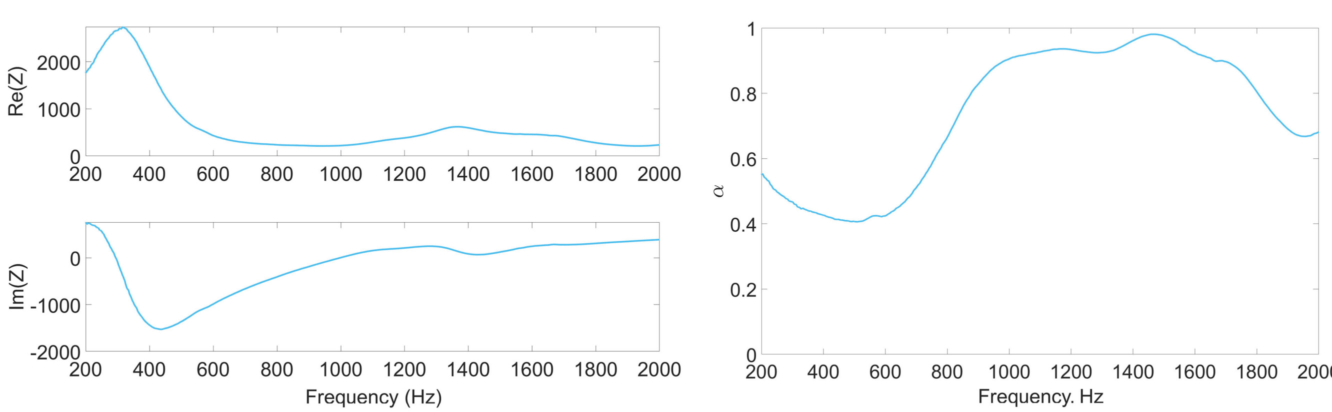

a) Impedance of the optimized T-Liner

b) Absorption of the optimized T-Liner

Fig. 14 Experimentally measured impedance and absorption coefficient of the optimized T-Liner: core and faceplate.

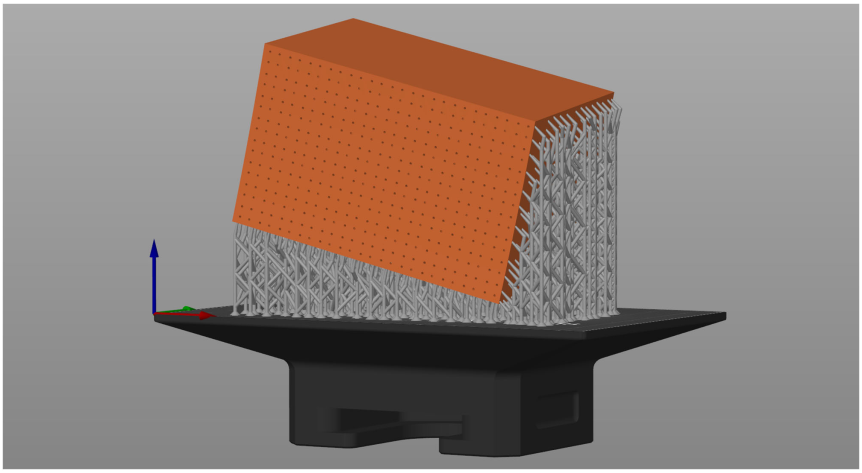

Fig. 15 Example of the print file for the ANCF T-liner sample B.

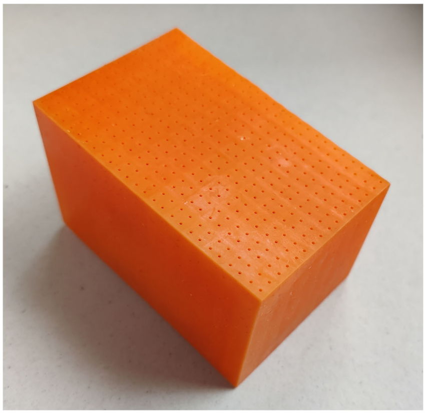

a) Top view of the T-liner

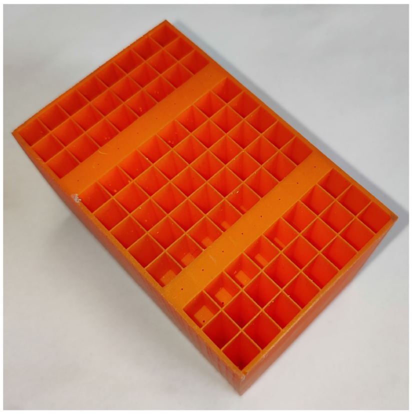

b) Bottom view of the T-liner

Fig. 16 Photograph of the MSLA 3D printed T-Liner design with integrated faceplate.

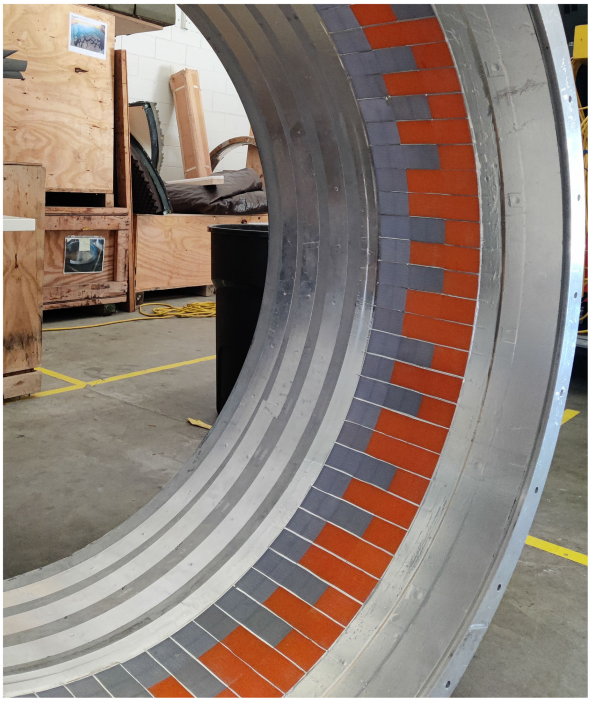

a) T-Liner installed in the ANCF liner casing

b) T-Liner installed in ANCF at the White Field test facility

Fig. 17 Photos of the 3D printed T-Liner used in ANCF testing.

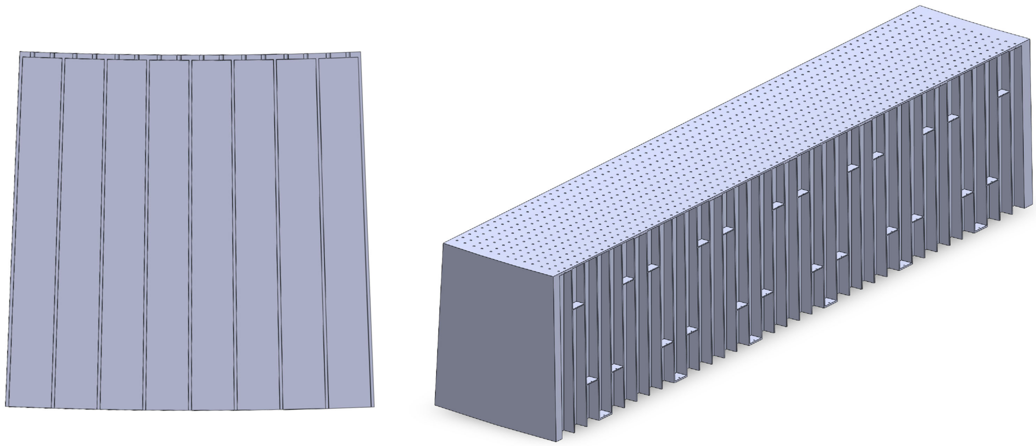

a) End view. 4.6° 8 cells wide

b) Isometric view. 6 unit cells+R1 in the streamwise direction. Approximately 228 mm long X 50 mm wide X 50.5 mm deep

Fig. 18 Final design of T-Liner accounting for ANCF curvature.

would be expected to have minimal impact on results. Each part was printed at a rate of 80 $cm^3 \cdot h^{-1}$ and it took approximately 480 h to manufacture the total amount. The total weight of the full liner, all 237 parts, was 9.4 kg.

V. Results

A. Normal Incidence

The normal incidence performance of the final metamaterial T-Liner design is presented in Fig. 19, which shows the absorption coefficient of the semi-analytical, experimental, and numerical data [39]. The results are compared to the experimental result of an optimized SDOF liner that was used as a benchmark for this testing. Both the T-Liner and SDOF liner went through equivalent optimization procedures, as described in Sec. III. Across the frequency range, the mean absorption coefficient of the T-Liner experimental result is $\overline{\alpha} = 0.74$; the mean absorption coefficient of the semi-analytical result is $\overline{\alpha} = 0.72$; and the mean absorption coefficient of the numerical result is $\overline{\alpha} = 0.72$. The mean absorption coefficient of the SDOF liner experimental result is $\overline{\alpha} = 0.51$. For all three sets of results of the T-Liner, the absorption coefficient is greater than 0.8 over a 1000 Hz range between 800 and 1.8 Hz. This is an excellent result and demonstrates the broadband, high absorption of the T-Liner in a low-frequency range. There is good agreement for all three results between 800 and 1200 Hz, and again at around the 1600 Hz peak. The semi-analytical and experimental results show more similarities in their behavior below 800 Hz than with the numerical results; however, it is the numerical and semi-analytical results that are in closer agreement between 1200 and 1600 Hz. In this frequency range, the numerical and semi-analytical results show a drop in the absorption coefficient to 0.8 and 0.84, respectively. Meanwhile, the experimental absorption coefficient remains above 0.92 in this range, with a peak absorption coefficient of 0.98 at 1465 Hz. Overall, the agreement between numerical, experimental, and analytical is extremely good; however, some differences are measured. For the experimental results, errors can result from nonperfectly circular holes in the 3D printing process and from printed diameters that differ from those designed due to aspects related to the exposure time and viscosity of the photosensitive resin. Errors in the analytical results at higher frequencies can occur when geometries are appreciable when compared to the wavelengths, thus violating inherent lumped model assumptions in the models. Errors in the numerical model can arise from errors and approximations in the boundary conditions and from meshing approximations.

In the SDOF experimental results, the spike in the absorption curve of the experimental results at 1550 Hz is caused by structural

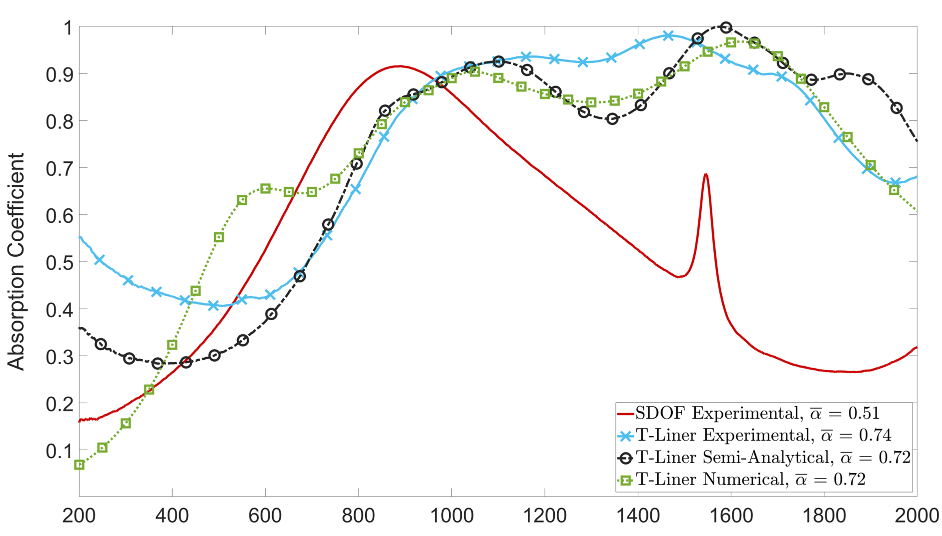

Fig. 19 Normal incidence T-Liner absorption coefficient compared to the benchmark SDOF design.

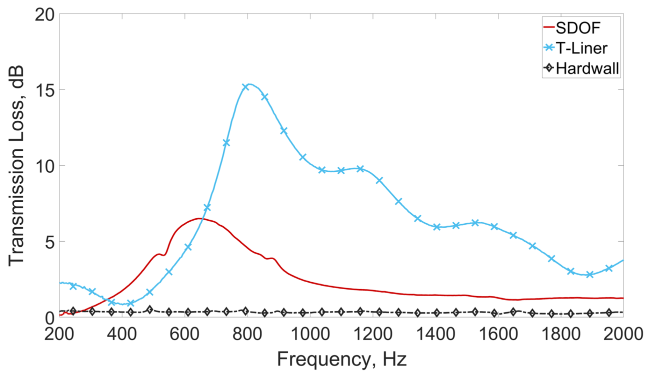

Fig. 20 Experimentally measured T-Liner transmission loss compared to the benchmark SDOF design.

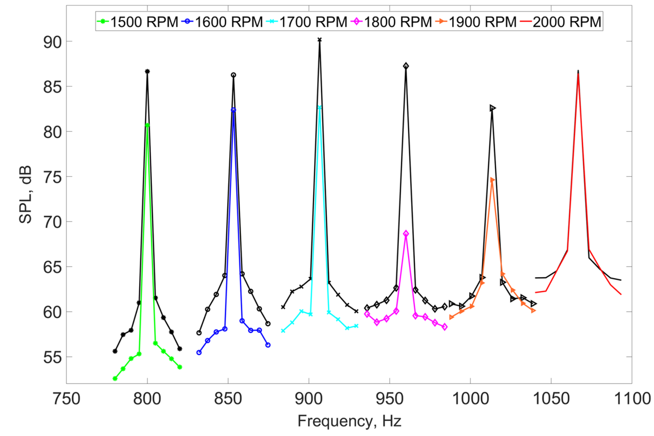

Fig. 22 Comparison of the hardwall and liner SPL in decibels at the 2BPF for each RPM test point.

vibrations of the microperforated plate [50]. This is not seen in the analytical or numerical results, as both of the predictive models only modeled the volume of the air and did not include the structural behaviors.

B. Grazing Incidence

Figure 20 shows the comparison of the experimentally measured transmission loss of the SDOF liner and the T-Liner. The SDOF liner experimental measurement has a transmission loss peak of 6.5 dB at 640 Hz. The T-Liner experimental measurement has a transmission loss peak of 15.2 dB at 810 Hz. Above 650 Hz, the T-Liner has a consistently higher transmission loss than the SDOF liner. Between 700 Hz and 1.2 kHz, the transmission loss of the T-Liner is greater than 8 dB. Above 1.2 kHz, there is a gradual reduction in amplitude from approximately 10 dB at 1.2 kHz to 5 dB at 1.7 kHz.

With a transmission loss peak at 810 Hz, 750–950 Hz is the approximate frequency range in which the liner is expected to perform best in the ANCF. However, the exact resonant frequency of the liner may be higher due to the magnitude of the incident acoustic wave (94 dB) and the flow conditions in the inlet. This was not investigated at this point, as the GIIT is not currently capable of testing with background flow conditions.

C. Advanced Noise Control Fan

Measurements were taken at 100 RPM increments between 1500 and 2000 RPM. Additionally, static tests were taken at 0 RPM. Measurements were performed for the full liner configuration, with the liner installed in the first spool section after the inlet section. A hardwall test was also performed at the same RPM test points that served as a benchmark. These measurements are the baseline configuration of the ANCF.

An example of the spectra for the baseline and liner configurations of the ANCF can be seen in Fig. 21. Both spectra are for the same test speed of 1800 RPM, which is the nominal speed of the ANCF, and for microphone location 13 at 43.5°. This microphone is chosen to provide an example of the frequency response and, as will be seen in the results, is the location at which the greatest tonal noise reduction occurs. The fan tones can be seen by the periodic sharp increases in the SPL; as discussed previously, these are a function of the number of blades in the fan, B, and occur at shaft orders that are integer multiples of B. The shaft order can be converted to frequency by multiplying by the test RPM and dividing by 60, RPM/60. As a result of this, the frequency at which the fan tones occur increases with increasing fan speed.

While the T-Liner is optimized to attenuate broadband noise below 2 kHz, testing in the GIIT shows that there is a specific frequency at which its performance is highest, as indicated by the transmission loss plot seen in Fig. 20. The T-liner will perform best at a test RPM where the frequency of a fan tone lies in this frequency range. In the preliminary testing in the GIIT, this occurred at approximately 750–950 Hz. However, in the ANCF, the incident acoustic pressure and flow conditions are different from the static testing in the GIIT. A direct comparison of the liner at each test speed is seen in Fig. 22. The 2BPF should occur at frequencies where the peak transmission loss was observed in the GIIT, so spectra centered on the 2BFP were isolated for each test speed between 1500 and 2000 RPM. The baseline for each test speed is shown in the solid black line for each speed. The most significant reduction is seen at the 1800 RPM test point, which is the nominal operating speed of the ANCF. This speed is the primary focus for a more in-depth analysis of the liner's performance for the entire microphone array.

To examine the impact of the acoustic liner on the noise generated by the fan of the ANCF, the difference in the SPL is obtained by subtracting the liner data from the baseline data for each microphone

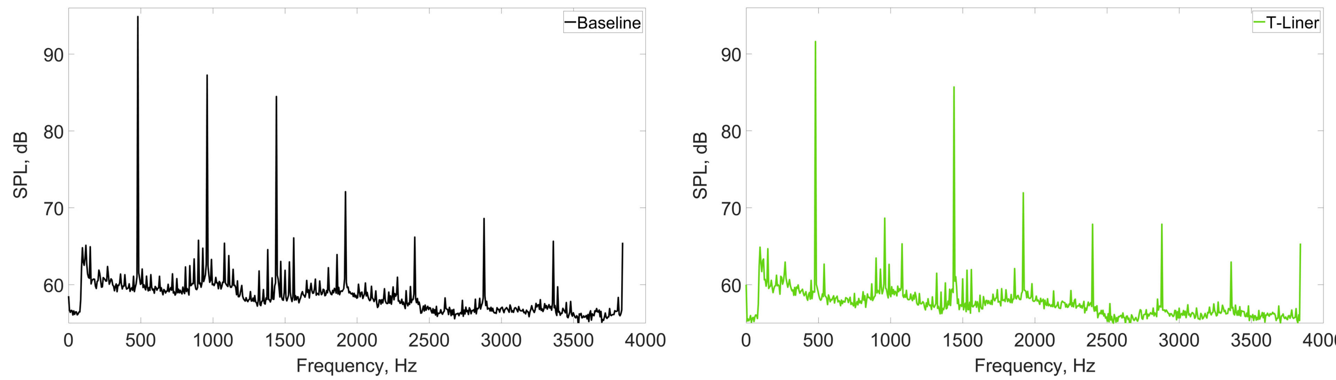

a) Hardwall baseline spectrum

b) T-Liner spectrum

Fig. 21 Example of the a) baseline and b) liner spectra of the ANCF at the nominal test speed of 1800 RPM.

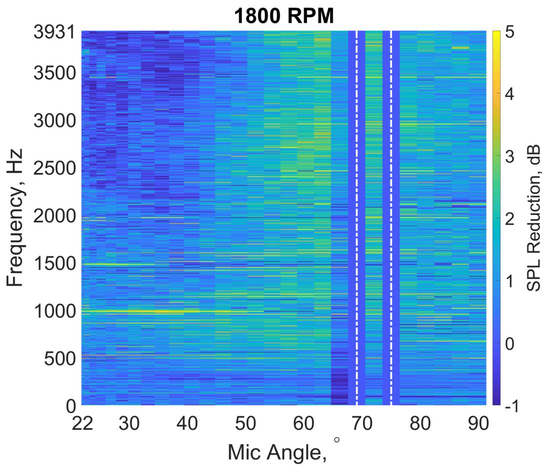

Fig. 23 Directivity plot of the difference in SPL between the baseline measurement and full liner measurement measured at 1800 RPM.

location. The initial analysis is performed on the data obtained at 1800 RPM. The resulting data set is used to generate the directivity plot in Fig. 23. The frequency in hertz is shown in the vertical axis; the azimuthal angle of the microphone location in degrees is given on the horizontal axis; and the magnitude of the plot is the SPL difference, Δ, in decibels, which is given by the color axis. Angles for microphone measurements are corrected to the azimuthal angle. A positive value for the SPL difference indicates where the liner reduced the noise. The white regions at 66 and 75° are caused by dead channels in the data acquisition system. To determine the average SPL across the full frequency range and for all microphone locations, the average pressure is calculated and converted to the SPL. The average SPL for the baseline configuration is 94.0 dB. The average SPL for the full-liner configuration is 91.4 dB; therefore, the resulting average SPL reduction by the liner is 2.6 dB. While the highest broadband noise reduction is observed at higher azimuthal angles, the liner reduces the tones generated by the first to third BPF significantly at lower azimuthal angles.

The first BPF occurs at approximately 480 Hz; the second BPF occurs at approximately 960 Hz; and the third BPF occurs at approximately 1440 Hz. At 1BPF, this is seen by the narrow orange-yellow line that extends to an azimuthal angle of 60°. This band is very narrow, which indicates that the subtones around the BPF are not significantly reduced by the liner, and the reductions are predominantly occurring at just the BPF tone. The thicker lines seen in yellow at the 2BPF and 3BPF indicate that the SPL reduction at these tones is also occurring at the subtones surrounding the BPF. For 2BPF, the greatest reductions are between an azimuthal angle of 30 and 40°. For 3BPF, the greatest reductions are between an azimuthal angle of 22 and 30°. However, above an azimuthal angle of 50°, there are more significant reductions in the broadband noise than tonal noise. This is indicated by the bright green to yellow region in the plot for frequencies about 2BPF.

The greatest tonal reductions were observed at microphone location 13 (mic13), corresponding to an azimuthal angle of 43.5°. The greatest overall broadband reduction was observed at microphone location 16 (mic16), corresponding to an azimuthal angle of 52°. The individual spectra at both locations, for both the baseline and liner configurations, are shown in Fig. 24. In Fig. 24a, the fundamental tone of the ANCF, located at 480 Hz, is reduced by 3.3 dB, and the first harmonic, located at 960 Hz, is reduced by 18.6 dB. Across the entire frequency range, the average total SPL reduction is 2.9 dB. In Fig. 24b, the fundamental tone is reduced by 3.5 dB, and the first harmonic is reduced by approximately 9.5 dB. The average SPL across the entire frequency range is reduced by 3.0 dB. The overall noise reduction across the frequency range and all microphone locations is 3.7 dB. The significant reduction of the first harmonic is expected as the harmonic occurs in approximately the same frequency range as the peak of the experimentally measured

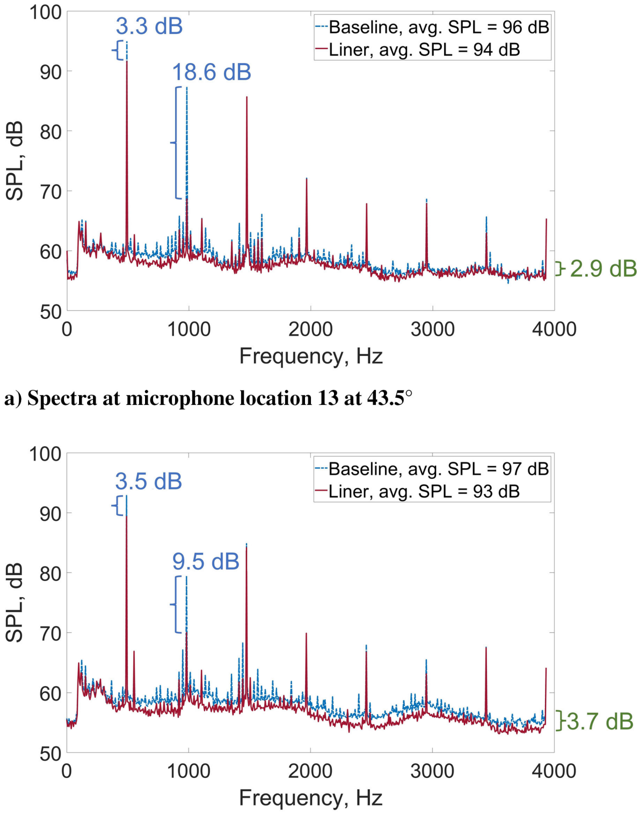

a) Spectra at microphone location 13 at 43.5°

b) Spectra at microphone location 16 at 52°

Fig. 24 Spectra for the individual microphone measurements at locations 13 and 16, at 1800 RPM.

transmission loss in Fig. 20. Repeatability of the measurements performed on the ANCF are examined in the Appendix.

1. Sound Power Level: Harmonic Bands

The sound power levels, PWL, as discussed in Sec. II.B.1, for each of the harmonic bands were determined by integrating the individual microphone spectra over each of the harmonic bands and multiplying by the area. The overall PWL for each of the harmonic bands are given in Fig. 25, along with the total PWL reduction across all harmonic bands. The tonal and broadband harmonic bands are given by Figs. 26 and 27, respectively, which separate the overall PWL into the tonal and broadband contributions. In Fig. 25, it can be seen that the greatest reductions to the overall PWL occur in the first and second harmonic bands. This is largely due to the significantly higher tonal PWL reductions that are achieved in these harmonic bands. In Fig. 27, it can be seen that the T-Liner has quite a consistent reduction

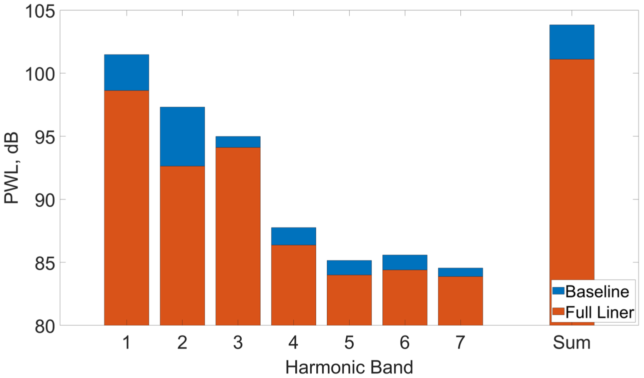

Fig. 25 Overall PWL of each of the harmonic bands for the T-Liner compared with the baseline measurements measured at 1800 RPM.

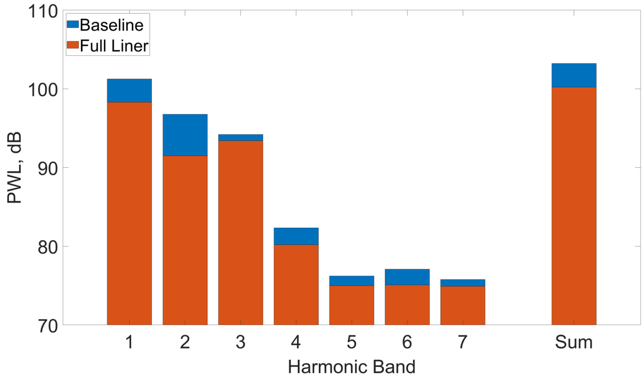

Fig. 26 Tonal PWL of each of the harmonic bands for the T-Liner compared with the baseline measurements measured at 1800 RPM.

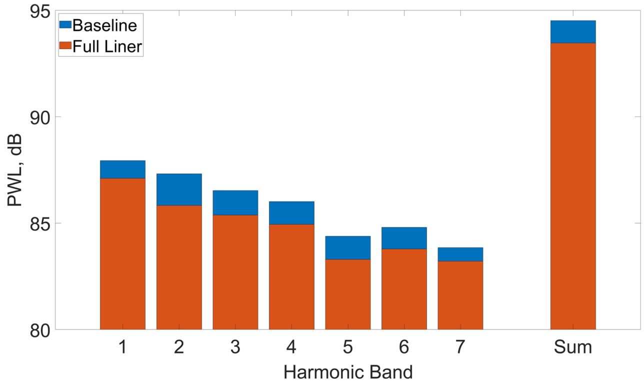

Fig. 27 Broadband PWL of each of the harmonic bands for the T-Liner compared with the baseline measurements measured at 1800 RPM.

in the broadband PWL. The greatest contribution to the overall reduction in the PWL is by the tonal PWL reduction in the second harmonic band, where there is a reduction of 5.3 dB, as seen in Fig. 26. As a result of this, the overall PWL reduction for the second harmonic band is 4.7 dB. Across all harmonic bands, there was a 2.7 dB reduction in the overall PWL, which is indicated by the sum data set in Fig. 25. The sum reduction in the tonal PWL across all harmonic bands is 3 dB, and the sum reduction in the broadband PWL is 1.1 dB.

Sutliff et al. [51] discussed the performance of SDOF liners in the ANCF, to which the T-Liner's performance can be compared. Three SDOF liners were installed, each measuring 457 mm (18 inches) in axial length, meaning that, in total, 1.37 m (54 inches) of acoustic treatment was installed. One liner section was installed in the inlet, one in the aft nacelle, and one in the aft centerbody. It was reported that the SDOF liner obtained a PWL attenuation of approximately 3 dB in the second to fifth harmonic bands in the forward far field. If it is assumed that it was the inlet section only of the SDOF liner that was responsible for PWL attenuation in the forward far-field testing, then it is observed that the T-Liner achieved a greater PWL attenuation with a liner half the length (228 mm vs 457 mm) of the SDOF liner. This shows the potential of the T-Liner concept to achieve high levels of noise attenuation, while still achieving size and weight savings.

VI. Conclusions

The T-liner design was optimized for normal impedance using a multistage optimization routine and was found to have an absorption coefficient of up to $\alpha = 0.97$ experimentally. It also has a broadband response with a mean absorption coefficient value of $\overline{\alpha} = 0.73$ in the 200–2000 Hz range. Optimization also benefited the SDOF liner design, which, with the same liner depth, achieved a mean absorption coefficient $\overline{\alpha} = 0.51$ for the same frequency range. This is a relatively good result compared to unoptimized SDOF designs, but clearly it does not have the capability of the AMDOF T-Liner for the same depth.

The T-liner was subsequently tested in the ANCF at a range of fan speeds and radiation angles. It is well understood that the optimum impedance of a liner in a grazing environment is frequency dependent. Nonetheless, given the low mean flow, the liner optimized for no-flow, normal incidence (i.e., targeting a ρc impedance) was considered to be acceptable. The liner performed best at the nominal operating speed of the ANCF, at 1800 RPM. At this speed, a tonal reduction of 18.6 dB at a radiation angle of 43.5° was measured. Both broadband and tonal noise PWL reductions of 1.1 and 3 dB, respectively, were achieved, with an overall PWL reduction of 2.7 dB across all harmonics achieved by the liner. With regard to efficiency, compared to previous results using an SDOF liner in the ANCF rig, the T-Liner has been shown to perform better at half the weight. Further work is required to investigate weight-to-efficiency ratios.

While the T-Liner performed well in testing in the ANCF, the broadband performance of the device and its ability to target multiple tones could be improved with a more complicated internal structure. In the design of the T-Liner presented, the variable geometry of the cells was highly repetitive, with the periodic location and geometry of the septa remaining consistent throughout the unit cell. A more complex optimization for multiple septa heights, and a septa thickness and perforation diameter that are tuned to each height separately could allow for a more broadband device. Additionally, the work presented here was conducted using relatively cheap SLA printers. The performance of the liner is affected by the quality of the print, and the use of a more precise printer would allow the quality of the samples and, therefore, the performance to be improved. Additionally, before the implementation of a similar device in an aircraft engine nacelle, the performance of the device would have to be assessed at a range of temperatures that are present in aircraft nacelles. It is now achievable to 3D print in metals, and therefore, as further advances in liner technology are made, 3D printed liners that can withstand the high temperatures of aeroengines are within grasp.

Appendix: Repeatability

To determine the repeatability of the measurement performed on the ANCF, the standard deviation across the measurements was determined. The standard deviation was determined using four data sets for the T-Liner measurements and eight data sets for the baseline measurements for each of the individual microphone locations. Data sets were collected over the course of two days of testing. In a single test run, two data sets were collected successively by varying the speed from 2000 RPM down to 1500 RPM in 100 RPM intervals and subsequently increasing the speed back up to 2000 RPM. Additional data sets for the baseline measurements were obtained during the test campaign for different liner treatments.

Figure A1 shows the standard deviation of the measurements at microphone location 13. Figure A2 shows the standard deviation of the measurements at microphone location 16. The sound pressure level in decibels is shown on the vertical axis, and the frequency in hertz is on the horizontal axis. The standard deviation of the full spectra for the entire frequency range for mic13 is seen in Fig. A1a, and the performance of the liner at the tones corresponding to 1BPF and 2BPF can be seen in Figs. A1b and A1c, respectively. Similarly, the standard deviation of the full spectra for mic16 is seen in Fig. A2a, and the performance of the liner at the tones corresponding to 1BPF and 2BPF can be seen in Figs. A2b and A2c, respectively.

The low standard deviation observed, particularly on the T-Liner data, shows a high degree of repeatability in the liner performance. In general, there is a gap between the upper limit of the liner standard deviation and the lower limit of the baseline standard deviation. This is not the case in the 2BPF tone observed at mic16 (shown in Fig. A2c); however, this is specifically seen at the tone, and in the broadband behavior (shown in Fig. A2a), there is a gap in the standard deviations of the liner and the baseline measurements.

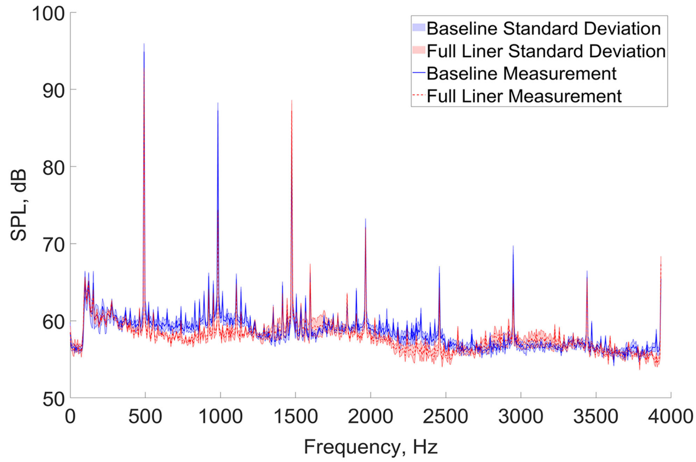

a) Standard deviation of the full spectra of mic13

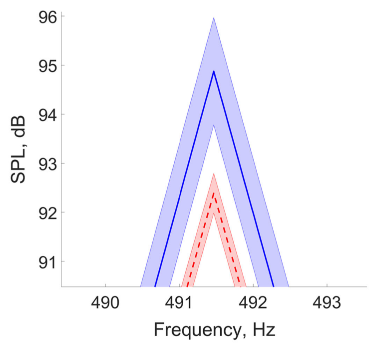

b) Standard deviation of the 1BPF

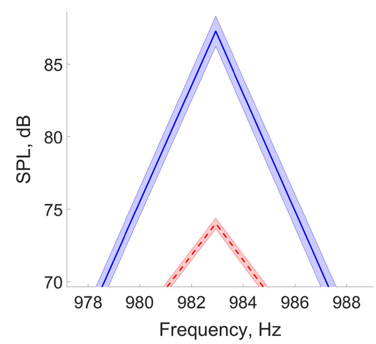

c) Standard deviation of the 2BPF

Fig. A1 Standard deviation of the baseline and liner measurements measured by mic13.

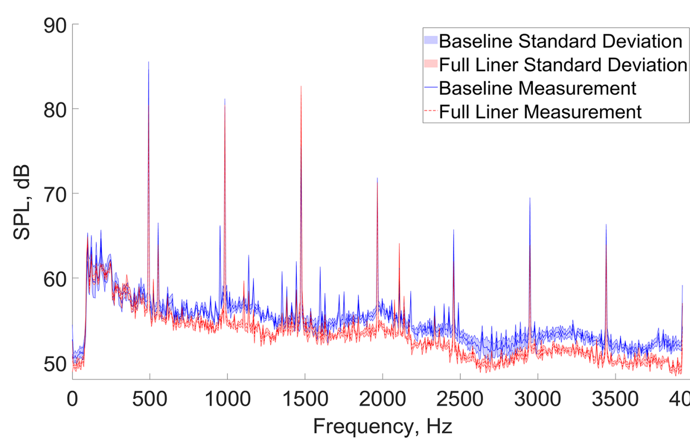

a) Standard deviation of the full spectra of mic16

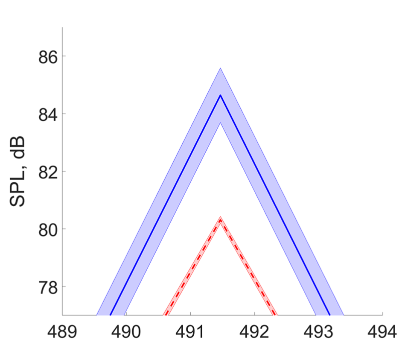

b) Standard deviation of the 1BPF

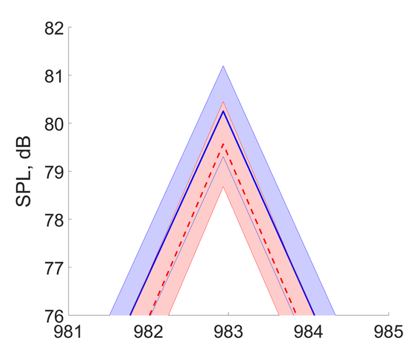

c) Standard deviation of the 2BPF

Fig. A2 Standard deviation of the baseline and liner measurements measured by mic16.

Acknowledgments

The authors would like to thank the Naughton Graduate Student Exchange Program of the Naughton Foundation for financially supporting this work. This project has also received funding from the European Union's Horizon 2020 research and innovation program under grant agreement number 860538 of the INVENTOR project. Additionally, the authors would like to thank the NASA Glenn Research Center and the Advanced Air Transport Technology Project/Power & Propulsion subproject for their support, both technical and financial, in the course of the testing. The staff of the Notre Dame Turbomachinery Laboratory is recognized for providing testing support on the Advanced Noise Control Fan.

References

[1] Hasegawa, T., "Effects of Novel Coronavirus (COVID-19) on Civil Aviation: Economic Impact Analysis," Sept. 2022, https://www.icao.int/sustainability/Documents/Covid-19/ICAO_coronavirus_Econ_Impact.pdf.

[2] "Air Passenger Numbers to Recover in 2024," IATA, March 2022, https://www.iata.org/en/pressroom/2022-releases/2022-03-01-01/.

[3] Theakston, F., "Burden of Disease from Environmental Noise: Quantification of Healthy Life Years Lost in Europe," World Health Organisation, 2011, OCLC: 779684347, https://apps.who.int/iris/handle/10665/326424.

[4] Black, D. A., Black, J. A., Issarayangyun, T., and Samuels, S. E., "Aircraft Noise Exposure and Resident's Stress and Hypertension: A Public Health Perspective for Airport Environmental Management," *Journal of Air Transport Management*, Vol. 13, No. 5, 2007, pp. 264–276, http://www.sciencedirect.com/science/article/pii/S0969699707000403.
https://doi.org/10.1016/j.jairtraman.2007.04.003

[5] Jarup, L., Dudley, M.-L., Babisch, W., Houthuijs, D., Swart, W., Pershagen, G., Bluhm, G., Katsouyanni, K., Velonakis, M., Cadum, E., et al., "Hypertension and Exposure to Noise Near Airports (HYENA): Study Design and Noise Exposure Assessment," *Environmental Health Perspectives*, Vol. 113, No. 11, 2005, pp. 1473–1478, http://www.ncbi.nlm.nih.gov/pmc/articles/PMC1310905/.
https://doi.org/10.1289/ehp.8037

[6] Sørensen, M., "Road Traffic Noise and Risk for Non-Hodgkin Lymphoma Among Adults," *EuroNoise*, Vol. 43, 2015, pp. 99–104.

[7] Zaporozhets, O., *Balanced Approach to Aircraft Noise Management*, Springer Nature, Cham, Switzerland, 2022, pp. 29–56.
https://doi.org/10.1007/978-3-030-91194-2_3

[8] Arnaldo Valdés, R. M., Burmaoglu, S., Tucci, V., Braga Da Costa Campos, L. M., Mattera, L., and Gomez Comendador, V. F., "Flight Path 2050 and ACARE Goals for Maintaining and Extending Industrial Leadership in Aviation: A Map of the Aviation Technology Space," *Sustainability*, Vol. 11, No. 7, 2019, p. 2065.
https://doi.org/10.3390/su11072065

[9] Neri, E., Kennedy, J., and Bennett, G. J., "Aeroacoustic Source Separation on a Full Scale Nose Landing Gear Featuring Combinations of Low Noise Technologies," *Internoise2015: Proceedings of the Internoise 2015/ASME NCAD Meeting*, American Soc. of Mechanical Engineers, San Francisco, 2015, Paper NCAD2015–5912, http://proceedings.asmedigitalcollection.asme.org/proceeding.aspx?articleid=2441119.
https://doi.org/10.1115/NCAD2015-5912

[10] Kennedy, J., Neri, E., and Bennett, G. J., "The Reduction of Main Landing Gear Noise," *22nd AIAA/CEAS Aeroacoustics Conference*, AIAA Paper 2016-2900, 2016.
https://doi.org/10.2514/6.2016-2900

[11] Neri, E., Kennedy, J., Di Giulio, M., O'Reilly, C., Dahan, J., Esposito, M., Bruno, M., Amoroso, F., Bianco, A., and Bennett, G. J., "Characterization of Low Noise Technologies Applied to a Full Scale Fuselage Mounted Nose Landing Gear," *Internoise2015: Proceedings of the Internoise 2015/ASME NCAD Meeting*, American Soc. of Mechanical Engineers, San Francisco, 2015, Paper NCAD2015–5911.
https://doi.org/10.1115/NCAD2015-5911

[12] Astley, R. J., "Can Technology Deliver Acceptable Levels of Aircraft Noise?" *INTER-NOISE and NOISE-CON Congress and Conference Proceedings*, 5, Vol. 249, Inst. of Noise Control Engineering, Washington, D.C., 2014, pp. 2622–2633.

[13] Pardowitz, B., Tapken, U., Knobloch, K., Bake, F., Bouty, E., Davis, I., and Bennett, G. J., "Core Noise—Identification of Broadband Noise Sources of a Turbo-Shaft Engine," *AIAA Aviation, 20th AIAA/CEAS Aeroacoustics Conference*, AIAA Paper 2014-3321, 2014.
https://doi.org/10.2514/6.2014-3321

[14] Bennett, G. J., and Fitzpatrick, J. A., "Noise-Source Identification for Ducted Fan Systems," *AIAA Journal*, Vol. 46, No. 7, 2008, pp. 1663–1674.
https://doi.org/10.2514/1.33522

[15] Dowling, A. P., and Mahmoudi, Y., "Combustion Noise," *Proceedings of the Combustion Institute*, Vol. 35, No. 1, 2015, pp. 65–100, https://linkinghub.elsevier.com/retrieve/pii/S1540748914004003.
https://doi.org/10.1016/j.proci.2014.08.016

[16] Sugimoto, R., Astley, R. J., and Murray, P. B., "Low Frequency Liners for Turbofan Engines," *20th International Congress on Acoustics*, Australian Acoustical Soc., Sydney, Australia, Aug. 2010, Paper 575, https://www.acoustics.asn.au/conference_proceedings/ICA2010/cdrom-ICA2010/papers/p575.pdf.

[17] McKay, A., Davis, I., Killeen, J., and Bennett, G. J., "SeMSA: A Compact Super Absorber Optimised for Broadband, Low-Frequency Noise Attenuation," *Scientific Reports*, Vol. 10, No. 1, 2020, p. 17967.

[18] Davis, I., McKay, A., and Bennett, G. J., "A Graph-Theory Approach to Optimisation of an Acoustic Absorber Targeting a Specific Noise Spectrum that Approaches the Causal Optimum Minimum Depth," *Journal of Sound and Vibration*, Vol. 505, Aug. 2021, Paper 116135, https://linkinghub.elsevier.com/retrieve/pii/S0022460X21002078.
https://doi.org/10.1016/j.jsv.2021.116135

[19] Killeen, J., Davis, I., Wang, J., and Bennett, G. J., "Fan-Noise Reduction of Data Centre Telecommunications' Server Racks, with an Acoustic Metamaterial Broadband, Low-Frequency Sound-Absorbing Liner," *Applied Acoustics*, Vol. 203, Feb. 2023, Paper 109229, https://linkinghub.elsevier.com/retrieve/pii/S0003682X23000270.
https://doi.org/10.1016/j.apacoust.2023.109229

[20] Hossain, M. R., Ross, E. P., and Bennett, G. J., "Acoustic Plate-Valve Resonator for Low-Frequency Sound Absorption," *AIP Advances*, Vol. 13, No. 6, 2023, Paper 065210, https://pubs.aip.org/adv/article/13/6/065210/2894744/Acoustic-plate-valve-resonator-for-low-frequency.
https://doi.org/10.1063/5.0142908

[21] Camussi, R., and Bennett, G. J., "Aeroacoustics Research in Europe: The CEAS-ASC Report on 2019 Highlights," *Journal of Sound and Vibration*, Vol. 484, Oct. 2020, Paper 115540, https://linkinghub.elsevier.com/retrieve/pii/S0022460X20303722.
https://doi.org/10.1016/j.jsv.2020.115540

[22] Palma, G., Mao, H., Burghignoli, L., Göransson, P., and Iemma, U., "Acoustic Metamaterials in Aeronautics," *Applied Sciences*, Vol. 8, No. 6, 2018, p. 971.
https://doi.org/10.3390/app8060971

[23] Liao, G., Luan, C., Wang, Z., Liu, J., Yao, X., and Fu, J., "Acoustic Metamaterials: A Review of Theories, Structures, Fabrication Approaches, and Applications," *Advanced Materials Technologies*, Vol. 6, No. 5, 2021, Paper 2000787.
https://doi.org/10.1002/admt.202000787

[24] Gao, N., Zhang, Z., Deng, J., Guo, X., Cheng, B., and Hou, H., "Acoustic Metamaterials for Noise Reduction: A Review," *Advanced Materials Technologies*, Vol. 7, No. 6, 2022, Paper 2100698.
https://doi.org/10.1002/admt.202100698

[25] Ma, G., and Sheng, P., "Acoustic Metamaterials: From Local Resonances to Broad Horizons," *Science Advances*, Vol. 2, No. 2, 2016, Paper e1501595.
https://doi.org/10.1126/sciadv.1501595

[26] Chen, S., Fan, Y., Fu, Q., Wu, H., Jin, Y., Zheng, J., and Zhang, F., "A Review of Tunable Acoustic Metamaterials," *Applied Sciences*, Vol. 8, No. 9, 2018, p. 1480, https://www.mdpi.com/2076-3417/8/9/1480.
https://doi.org/10.3390/app8091480

[27] Jones, M. G., Nark, D. M., and Howerton, B. M., "Overview of Liner Activities in Support of the International Forum for Aviation Research," *25th AIAA/CEAS Aeroacoustics Conference*, AIAA Paper 2016-2599, 2019.
https://doi.org/10.2514/6.2019-2599

[28] Wang, J., Bennett, G. J., Humbert, T., Auregan, Y., Åbom, M., and Boden, H., "Low-Frequency Broadband Noise Absorption of Multi-Chamber Micro-Perforated Pane Absorbers in Normal and Grazing Acoustic Incidence," *AIAA Aviation 2023 Forum*, AIAA Paper 2023-3829, 2023.
https://doi.org/10.2514/6.2023-3829

[29] Boden, H., Sack, S., and Jacob, S., "Impedance Measurements for 3-D Printed Liners," *25th AIAA/CEAS Aeroacoustics Conference*, AIAA Paper 2019-2600, 2019.
https://doi.org/10.2514/6.2019-2600

[30] Bake, F., Burgmayer, R., Schulz, A., and Enghardt, L., "IFAR Liner Benchmark—Challenge #1—DLR," *25th AIAA/CEAS Aeroacoustics Conference*, AIAA Paper 2019-2601, 2019.
https://doi.org/10.2514/6.2019-2601

[31] Ishii, T., Nagai, K., Oinuma, H., and Enomoto, S., "Experimental Study of Acoustic Liner Panels Shared in IFAR Program," *25th AIAA/CEAS Aeroacoustics Conference*, AIAA Paper 2019-2602, 2019.
https://doi.org/10.2514/6.2019-2602

[32] Wong, J., Nesbitt, E., Jones, M. G., and Nark, D. M., "Flight Test Methodology for NASA Advanced Inlet Liner on 737MAX-7 Test Bed (Quiet Technology Demonstrator 3)," *25th AIAA/CEAS Aeroacoustics Conference*, AIAA Paper 2019-2763, 2019.
https://doi.org/10.2514/6.2019-2763

[33] Nark, D. M., and Jones, M. G., "Design of an Advanced Inlet Liner for the Quiet Technology Demonstrator 3," *25th AIAA/CEAS Aeroacoustics Conference*, AIAA Paper 2019-2764, 2019.
https://doi.org/10.2514/6.2019-2764

[34] Nark, D. M., and Jones, M. G., "An Acoustic Liner Design Methodology Based on a Statistical Source Model," *International Journal of Aeroacoustics*, Vol. 20, Nos. 5–7, 2021, pp. 441–457.
https://doi.org/10.1177/1475472X211023874

[35] Sutliff, D. L., Nark, D. M., and Jones, M. G., "Multi-Degree-of-Freedom Liner Development: Concept to Flight Test," *International Journal of Aeroacoustics*, Vol. 20, Nos. 5–7, 2021, pp. 792–825.
https://doi.org/10.1177/1475472X211023860

[36] Sutliff, D. L., "A 20 Year Retrospective of the Advanced Noise Control Fan—Contributions to Turbofan Noise Research," AIAA Paper 2019-3824, 2019.
https://doi.org/10.2514/6.2019-3824

[37] "Standard Test Method for Measurement of Normal Incidence Sound Transmission of Acoustical Materials Based on the Transfer Matrix Method," ASTM International, Vol. ASTM E2611-09, 2009.

[38] "ISO 15034-2:2001, Acoustics—Determination of Sound Absorption Coefficient and Impedance in Impedance Tubes—Part 2: Transfer-function Method," ISO Standards, 2001.

[39] Ross, E. P., Figueroa-Ibrahim, K. M., Sutliff, D. L., Morris, S., and Bennett, G. J., "Evaluation of an Additive-Manufactured Acoustic Metamaterial as an Nacelle Liner Using the Active Noise Control Fan," *AIAA Aviation 2023 Forum*, AIAA Paper 2023-3827, 2023.
https://doi.org/10.2514/6.2023-3827

[40] Figueroa-Ibrahim, K. M., Morris, S., Ross, M., and Sutliff, D. L., "Evaluation of Radiated Sound from the Advanced Noise Control Fan Facility in an Outdoor Environment Using Ground Microphones," AIAA Paper 2019-3825, 2019.
https://doi.org/10.2514/6.2019-3825

[41] McAllister, J., Loew, R., Lauer, J., and Sutliff, D., "The Advanced Noise Control Fan Baseline Measurements," *47th AIAA Aerospace Sciences Meeting Including the New Horizons Forum and Aerospace Exposition*, AIAA Paper 2009-0624, 2009.
https://doi.org/10.2514/6.2009-624

[42] Tang, Y., Ren, S., Meng, H., Xin, F., Huang, L., Chen, T., Zhang, C., and Lu, T. J., "Hybrid Acoustic Metamaterial as Super Absorber for Broadband Low-Frequency Sound," *Scientific Reports*, Vol. 7, No. 1, 2017, Paper 43340, http://www.nature.com/articles/srep43340.
https://doi.org/10.1038/srep43340

[43] Parrott, T. L., and Jones, M. G., "Parallel-Element Liner Impedances for Improved Absorption of Broadband Sound in Ducts," *Noise Control Engineering Journal*, Vol. 43, No. 6, 1995, pp. 183–195.

[44] Maa, D.-Y., "Potential of Microperforated Panel Absorber," *Journal of the Acoustical Society of America*, Vol. 104, No. 5, 1998, pp. 2861–2866.
https://doi.org/10.1121/1.423870

[45] Fok, V., "Teoreticheskoe Issledovanie Provodimosti Kruglogo Otverstiya v Peregorodke, Postavlennoi Poperek Truby [Theoretical Study of the Conductance of a Circular Hole in a Partition Across a Tube]," *Doklady Akademii Nauk SSSR (Soviet Physics Doklady)*, Vol. 31, No. 9, 1941, pp. 875–882.

[46] Wang, J., and Bennett, G. J., "Multi-Chamber Micro-Perforated Panel Absorbers Optimised for High Amplitude Broadband Absorption Using a Two-Point Impedance Method," *Journal of Sound and Vibration*, Vol. 547, March 2023, Paper 117527, https://linkinghub.elsevier.com/retrieve/pii/S0022460X22007106.
https://doi.org/10.1016/j.jsv.2022.117527

[47] Wang, J., and Bennett, G. J., "Ultra-Broadband Sound Absorption in a Compact Multi-Chamber Micro-Perforated Panel Absorber with Varying Depths," *AIP Advances*, Vol. 14, No. 1, 2024, Paper 015009, https://pubs.aip.org/adv/article/14/1/015009/2932464/Ultra-broadband-sound-absorption-in-a-compact.
https://doi.org/10.1063/5.0187328

[48] Oda, G., Miyoshi, T., Takaya, Y., Ha, T., and Kimura, K., "Microfabrication of Overhanging Shape Using LCD Microstereolithography," *SPIE Proceedings*, edited by I. Miyamoto, H. Helvajian, K. Itoh, K. F. Kobayashi, A. Ostendorf, and K. Sugioka, SPIE Digital Library, Bellingham, WA, 2004, pp. 649–654, http://proceedings.spiedigitallibrary.org/proceeding.aspx?articleid=857538.
https://doi.org/10.1117/12.596758

[49] Ross, E., "A 3D Printed Acoustic Metamaterial Liner to Reduce Low-Frequency Aeroengine Noise," Ph.D. Thesis, Trinity College Dublin, Univ. of Dublin, Dublin, 2023.

[50] Temiz, M. A., Tournadre, J., Lopez Arteaga, I., and Hirschberg, A., "Modelling Vibro-Acoustic Coupling in Flexible Micro-Perforated Plates by a Patch-Impedance Approach," *Applied Acoustics*, Vol. 125, Oct. 2017, pp. 80–90, https://linkinghub.elsevier.com/retrieve/pii/S0003682X16304182.
https://doi.org/10.1016/j.apacoust.2017.04.012

[51] Sutliff, D. L., Bozak, R. F., Jones, M. G., and Nark, D. M., "Investigations of Three Over-the-Rotor Liner Concepts at Various Technology Readiness Levels," *International Journal of Aeroacoustics*, Vol. 20, Nos. 5–7, 2021, pp. 826–866.
https://doi.org/10.1177/1475472X211025803

X. Zhang
Associate Editor